Change in Microphase-separated Structure and Macroscopic Mechanical Response of Styrenic Triblock Copolymer during Various Deformation Modes

ナッタニー, デートナロン

九州大学
KYUSHU UNIVERSITY

Deformation Mechanism of Microphase-separated Structure of Styrenic Triblock Copolymer during Various Mechanical Deformation Modes

By

Nattanee Dechnarong

A thesis submitted in partial fulfillment
of the requirements for the degree of
Doctor of Engineering

Department of Chemistry and Biochemistry
Graduate School of Engineering
Kyushu University
Fukuoka, Japan

2021

TABLE OF CONTENTS

LIST OF FIGURES

LIST OF TABLES

Chapter 1

Introduction

1.1 Introduction

For elastomeric materials, cross-linking points play an important role in controlling their mechanical properties. There are two types of cross-linking points: chemical and physical cross-links. Figure 1.1 shows schematic illustration of chemical and physical cross-link points of elastomers. An elastomer cross-linked by chemical bonding with optimal cross-linking density exhibits excellent mechanical properties. However, chemical bonding is considered a drawback in rubber waste management, which is currently an environmental concern. Accordingly, thermoplastic elastomers (TPEs) have become alternative elastomeric materials. Physical cross-links are incorporated in the structure of TPEs to provide elastomeric properties with the processability of thermoplastic materials. Thus, the ability to recycle TPEs has made them an attractive alternative.

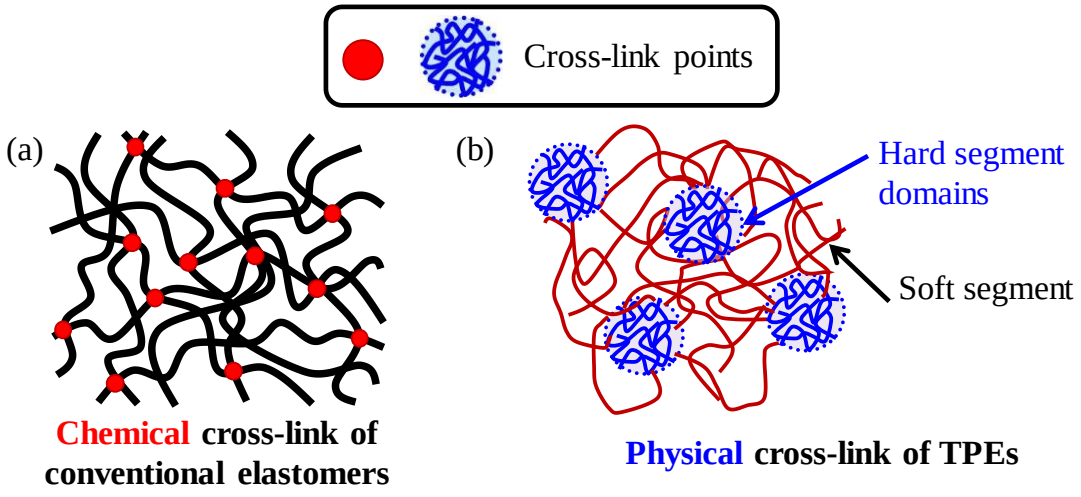

Figure 1.1. Schematic illustration of (a) chemical and (b) physical cross-link points.

There are various types of TPEs, including polyolefin blends, copolyesters, polyurethanes, polyamides and styrenic block copolymers. Styrenic-based block copolymers are one of the largest consumed TPEs in the market since their properties can benefit a variety of applications. Microphase separation can be induced in

styrenic-based block copolymers, which imparts interesting properties on the block copolymers.[1-7] Microphase-separated morphology is typically based on the inclusion of a fraction of polystyrene (PS) depending on application.[8-10] Poly(styrene-*b*-ethylene-*co*-butylene-*b*-styrene) (SEBS) is a commercial styrenic triblock copolymer used in various applications. Chemical structure of SEBS is illustrated in Figure 1.2. SEBS is synthesized from hydrogenated PS-*b*-polybutadiene-*b*-PS (SBS). Since the midsegment of the precursor polymer consisted of 1,4- and 1,2-additions of butadiene, 1,4-butylene (two ethylenes) and 1,2-butylene units were produced after hydrogenation. Due to being a saturated hydrocarbon, SEBS shows oxidative resistance properties, which is an advantage over other well-known styrenic triblock copolymers, such as SBS and PS-*b*-polyisoprene-*b*-PS (SIS). The fraction of rubbery poly(ethylene-*co*-butylene) (PEB) midblocks and glassy PS end blocks regulates the properties of SEBS. Figure 1.3 shows schematic illustration of microphase-separated structure of SEBS. The PS domains are the physical cross-link points in the PEB matrix. Chain conformation of the midblock segment is one of the main factors that influence the deformation mechanism of ABA triblock copolymers. There are two types of midblock structures: bridge and loop chains.[11-14] Bridge chains are segments that connect different PS domains, whereas loop chains are segments in the same PS domain.

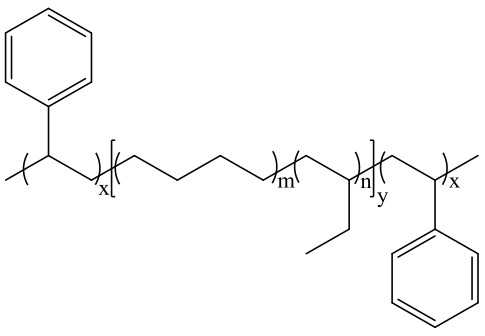

Figure 1.2. Chemical structure of the SEBS triblock copolymer.

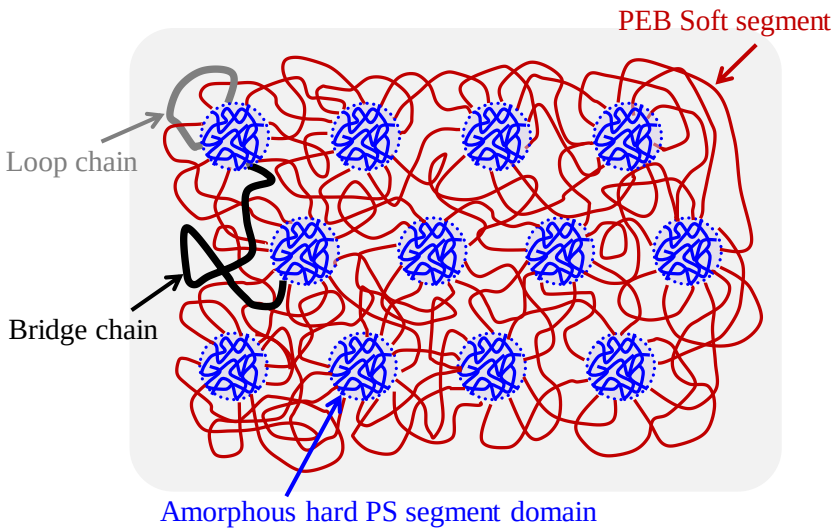

Figure 1.3. Schematic illustration of microphase-separated structure of SEBS.

Elastic property is a property that materials can recover to their initial shape and size after removing an external force. In polymers, the elasticity originates from their network structures. Two origins of the elastic property are retractive force and entropy of the polymer network. During stretching, polymer chains changed their conformation, leading to a decrement of entropy. This change in entropy produces retractive force, which governs elastic property of the polymers.[15] For the cross-linking points, they are important in terms of retaining the network structure, leading to be a role to control the mechanical properties of elastomers. Therefore, the mechanical stability of PS domains in SEBS is a key point for improving the mechanical strength and toughness of SEBS. The orientation of the PEB chains during sample deformation is also crucial for understanding the mechanical properties of the material. To understand the deformation mechanism of a material, it is essential to determine its deformation behaviors under several deformation modes. Although the uniaxial tensile test is a fundamental elongation mode, discussion based on only uniaxial elongation mode is insufficient for explaining the deformation behavior of a material in terms of practical aspect. Equi-biaxial

stretching as well as compression and bulge test are among efficient tests to conduct in comparison with uniaxial stretching, as information from these modes can yield information on many aspects of nonlinear stress-strain behaviors.[16-18] Furthermore, behaviors of the material during loading-unloading process are also important to investigate as a change in stress-strain properties from the first extension was reported in elastomer materials. The change in properties of the sample during loading-unloading process could highlight the occurrence of irreversible structure change in the sample.

Small-angle X-ray scattering (SAXS) and wide-angle X-ray scattering (WAXS) are well-established techniques to investigate the small-scale structure and fluctuations in soft matter. SAXS is widely used to probe the morphology of semicrystalline block copolymers at the level of the microphase separated structure, while WAXS is used to examine crystalline structure. The high photon flux and collimation provided by modern synchrotron sources has made SAXS/WAXS unique scattering techniques in terms of time resolution, small sample volume, *etc*. Time-resolved experiments down to millisecond range can be performed on bulk as well as even on dilute and low contrast samples. Therefore, *in situ* SAXS/WAXS techniques are powerful methods to investigate the microphase-separated structure of block copolymers during mechanical deformations. Many studies have reported on the deformation behavior of various types of thermoplastic elastomers based on these techniques.[19-29] Kawai *et al*. were the first researchers to publish about the deformation mechanism of block copolymers using simultaneous small angle light scattering and SAXS measurements.[19] PS-*b*-polyisoprene (SI) and SIS with spherical PS domains as the linking points were uniaxially stretched. They concluded that the interdomain distance increased with increasing strain in the stretching direction, as observed from a change in the scattering intensity distribution from the SAXS results.

In this study, *in situ* SAXS/WAXS measurements were performed to investigate the microphase-separated structure of SEBS during various deformation modes. Figure 1.4 shows the experimental set-up of *in situ* synchrotron radiation X-ray scattering measurement during mechanical test in SPring-8, Japan. An arrangement and deformation behaviors of PS domains during various deformation modes were investigated using *in situ* SAXS measurement. An orientation of the PEB chains was investigated using *in situ* WAXS measurement.

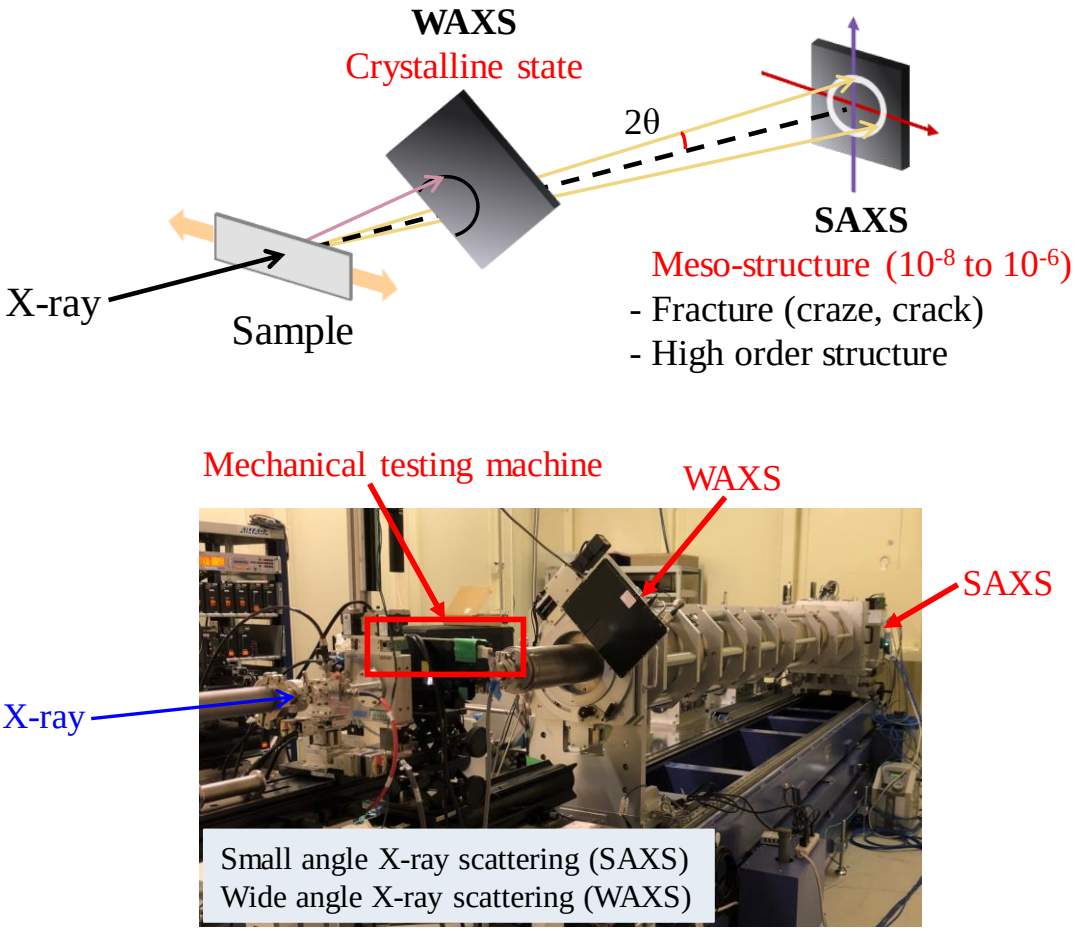

Figure 1.4. Experimental set-up of *in situ* SAXS/WAXS measurements.

1.2 Structure of thesis

In Chapter 2, changes in the microphase-separated structure of the SEBS triblock copolymer (13 wt% PS block) were investigated. *In situ* synchrotron radiation

SAXS/WAXS measurements were successfully performed for SEBS under equi-biaxial deformation as well as under uniaxial deformation. *In situ* SAXS/WAXS measurements revealed changes in (1) the shape of spherical PS domains, (2) the spacing of PS domains packed in the body-centered cubic structure in the initial state, (3) their ordering, and (4) the orientation of soft segment chains during deformations. In terms of the microdomain structure, affine deformation was kept below a certain strain ($\mathcal{E}_{\text{d-A}}$), which are 4 and 1.2, during uniaxial and equi-biaxial deformation, respectively. In contrast, the ordering of arranged PS domain decreased from initial strain region. Above the $\mathcal{E}_{\text{d-A}}$ value, deviation from affine deformation started to occur. This deviation is related to contact of PS domains under mechanical deformation. Uniaxial stretching still showed the plane-independent phenomenon, while equi-biaxial stretching did not. Furthermore, the $\mathcal{E}_{\text{d-A}}$ value for equi-biaxial deformation is smaller than for uniaxial deformation and further smaller than expected. This is maybe because entanglement effect is enhanced for equi-biaxial deformation. Furthermore, after contact of PS domains at around strain of 6 and 2, during uniaxial and equi-biaxial deformation, respectively, the ordering of PS domains suddenly increased with an increase in strain. It is inferred that the locked state between the PS domains and the extended PEB chains formed during deformation may have been released and repacked at a certain strain.

In Chapter 3, the mechanical stretching behavior of SEBS was investigated under three different stretching modes and through *in situ* SAXS analysis. Strain energy density function was investigated based on the stress and stretching ratio (λ) relationship under uniaxial, planar extension, and equi-biaxial stretching modes. As a result, the cross-effect of strain represented by second invariants of the deformation tensor (I_2) was identified, and only the Ogden model could be used to fit the data. In the cyclic stretching test, SEBS exhibited smaller hysteresis during cyclic equi-biaxial stretching than that during

uniaxial stretching. In other words, the Mullins effect was more obvious for uniaxial stretching than biaxial stretching. The λ and stretching ratio obtained from crystal planes by SAXS (λ_{SAXS}) were compared to investigate the relationship between the microdomain structure change and macroscopic mechanical properties. Thus, it was revealed that affine deformation occurred in the smaller λ region for both uniaxial and equi-biaxial stretching and deviation from affine deformation occurred for the uniaxial stretching at the larger λ region. This is because PEB with entangled loops served as cross-linking points when the films were stretched under the equi-biaxial stretching.

In Chapter 4, apart from a well-known equi-biaxial testing, SEBS during compression and bulge tests were investigated. SAXS results revealed simple arrangement of PS domains at small strain during equi-biaxial stretching and bulge test. However, simple arrangement was not observed during compression test. The samples during bulge and compression tests were suggested to deform in multiaxial directions as the applied force acting on each sample was different from equi-biaxial stretching. Correlation between the results of bulged and compressed sample observed from through view was found. Different characteristic of 2d-SAXS patterns was found in each deformation mode. Explanation was discussed based on the calculation of scattering pattern using Fast Fourier Transform (FFT). Dot-like pattern was clearly observed in bulge test, suggesting the occurrence of large grain. On the contrary, equi-biaxial stretching and compression test exhibited the combination of line-like and dot-like pattern, indicating the combination of different grain size. For the deformation of PS domains, the results of form factor revealed that the spherical PS domains transformed to oblate spheroid during these three modes.

1.3 References

(1) Matsuo, M.; Ueno, T.; Horino, H.; Chujyo, S.; Asai, H. Fine structures and physical properties of styrene-butadiene block copolymers. *Polymer* **1968**, *9*, 425-436.

(2) Leibler, L. Theory of microphase separation in block copolymers. *Macromolecules* **1980**, *13*, 1602-1617.

(3) Adams, J. L.; Quiram, D. J.; Graessley, W. W.; Register, R. A.; Marchand, G. R. Ordering dynamics of compositionally asymmetric styrene−isoprene block copolymers. *Macromolecules* **1996**, *29*, 2929-2938.

(4) Heck, B.; Arends, P.; Ganter, M.; Kressler, J.; Stühn, B. SAXS and TEM studies on poly (styrene)-block-poly (ethene-co-but-1-ene)-block-poly (styrene) in bulk and at various interfaces. *Macromolecules* **1997**, *30*, 4559-4566.

(5) Sohn, K. E.; Kojio, K.; Berry, B. C.; Karim, A.; Coffin, R. C.; Bazan, G. C.; Kramer, E. J.; Sprung, M.; Wang, J. Surface effects on the thin film morphology of block copolymers with bulk order−order transitions. *Macromolecules* **2010**, *43*, 3406-3414.

(6) Pester, C. W.; Schmidt, K.; Ruppel, M.; Schoberth, H. G.; Böker, A. Electric-field-induced order–order transition from hexagonally perforated lamellae to lamellae. *Macromolecules* **2015**, *48*, 6206-6213.

(7) Tan, X.; Li, J.; Guo, S. Temperature-dependent order-to-order transition of polystyrene-block-poly(ethylene-co-butylene)-block-polystyrene triblock copolymer under multilayered confinement. *Macromolecules* **2018**, *51*, 2099-2109.

(8) Ohta, T.; Kawasaki, K. Equilibrium morphology of block copolymer melts. *Macromolecules* **1986**, *19*, 2621-2632.

(9) Mita, K.; Tanaka, H.; Saijo, K.; Takenaka, M.; Hashimoto, T. Cylindrical domains of block copolymers developed via ordering under moving temperature gradient. *Macromolecules* **2007**, *40*, 5923-5933.

(10) Ahn, S.; Seo, Y.; Kim, J. K.; Duan, C.; Zhang, L.; Li, W. Cylindrical to lamellar microdomain transition upon heating for a linear tetrablock copolymer with upper critical ordering transition. *Macromolecules* **2019**, *52*, 9039-9044.

(11) Gaylord, R. J.; Lohse, D. J. Block copolymer deformation. *Polym. Eng. Sci.* **1978**, *18*, 359-365.

(12) Gehlsen, M. D.; Almdal, K.; Bates, F. S. Order-disorder transition: diblock versus triblock copolymers. *Macromolecules* **1992**, *25*, 939-943.

(13) Watanabe, H.; Sato, T.; Osaki, K. Concentration dependence of loop fraction in styrene−isoprene−styrene triblock copolymer solutions and corresponding changes in equilibrium elasticity. *Macromolecules* **2000**, *33*, 2545-2550.

(14) Watanabe, H.; Matsumiya, Y.; Sawada, T.; Iwamoto, T. Rheological and dielectric behavior of dipole-inverted (SIS)p-type multiblock copolymers: estimates of bridge/loop fractions for respective I blocks and effect of loops on high extensibility of bridges. *Macromolecules* **2007**, *40*, 6885-6897.

(15) Strobl, G. R., The physics of polymers. 3^{ed}.; Springer: 1997.

(16) Bitoh, Y.; Akuzawa, N.; Urayama, K.; Takigawa, T. Strain energy function of swollen polybutadiene elastomers studied by general biaxial strain testing. *J. Polym. Sci. Part B: Polym. Phys.* **2010**, *48*, 721-728.

(17) Yohsuke, B.; Urayama, K.; Takigawa, T.; Ito, K. Biaxial strain testing of extremely soft polymer gels. *Soft Matter* **2011**, *7*, 2632-2638.

(18) Krishnan, A. S.; Van Zanten, J. H.; Seifert, S.; Lee, B.; Spontak, R. J. Selectively solvated triblock copolymer networks under biaxial strain. *Appl. Phys. Lett.* **2011**, *99*, 101908.

(19) Inoue, T.; Moritani, M.; Hashimoto, T.; Kawai, H. Deformation mechanism of elastomeric block copolymers having spherical domains of hard segments under uniaxial tensile stress. *Macromolecules* **1971**, *4*, 500-507.

(20) Brandt, M.; Ruland, W. SAXS studies on the deformation of macrolattices in block copolymers. *Acta Polym.* **1996**, *47*, 498-506.

(21) Huy, T. A.; Adhikari, R.; Michler, G. H. Deformation behavior of styrene-block-butadiene-block-styrene triblock copolymers having different morphologies. *Polymer* **2003**, *44*, 1247-1257.

(22) Stribeck, N.; Fakirov, S.; Apostolov, A. A.; Denchev, Z.; Gehrke, R. Deformation behavior of PET, PBT and PBT-based thermoplastic elastomers as revealed by SAXS from synchrotron. *Macromol. Chem. Phys.* **2003**, *204*, 1000-1013.

(23) Kojio, K.; Nakamura, S.; Furukawa, M. Effect of side methyl groups of polymer glycol on elongation-induced crystallization behavior of polyurethane elastomers. *Polymer* **2004**, *45*, 8147-8152.

(24) Kojio, K.; Nakamura, S.; Furukawa, M. Effect of side groups of polymer glycol on microphase-separated structure and mechanical properties of polyurethane elastomers. *J. Polym. Sci. Part B: Polym. Phys.* **2008**, *46*, 2054-2063.

(25) Kojio, K.; Matsuo, K.; Motokucho, S.; Yoshinaga, K.; Shimodaira, Y.; Kimura, K. Simultaneous small-angle X-ray scattering/wide-angle X-ray diffraction study of the microdomain structure of polyurethane elastomers during mechanical deformation. *Polym. J.* **2011**, *43*, 692.

(26) Matsumiya, Y.; Watanabe, H.; Takano, A.; Takahashi, Y. Uniaxial extensional behavior of (SIS)p-type multiblock copolymer systems: structural origin of high extensibility. *Macromolecules* **2013**, *46*, 2681-2695.

(27) McCready, E. M.; Burghardt, W. R. In situ SAXS studies of structural relaxation of an ordered block copolymer melt following cessation of uniaxial extensional flow. *Macromolecules* **2015**, *48*, 264-271.

(28) Tomita, S.; Lei, L.; Urushihara, Y.; Kuwamoto, S.; Matsushita, T.; Sakamoto, N.; Sasaki, S.; Sakurai, S. Strain-induced deformation of glassy spherical microdomains in elastomeric triblock copolymer films: simultaneous measurements of a stress–strain curve with 2d-SAXS patterns. *Macromolecules* **2017**, *50*, 677-686.

(29) Higaki, Y.; Suzuki, K.; Kiyoshima, Y.; Toda, T.; Nishiura, M.; Ohta, N.; Masunaga, H.; Hou, Z.; Takahara, A. Molecular aggregation states and physical properties of syndiotactic polystyrene/hydrogenated polyisoprene multiblock copolymers with crystalline hard domain. *Macromolecules* **2017**, *50*, 6184-6191.

Chapter 2

Deformation mechanism during simple uniaxial and equi-biaxial stretching modes

2.1 Introduction

To understand the deformation mechanism of a material, it is essential to determine its deformation behaviors under several deformation modes. Although the uniaxial tensile test is a fundamental elongation mode, discussion based on only uniaxial elongation mode is insufficient for explaining the deformation behavior of a material in terms of practical aspect. Equi-biaxial stretching is one of the most efficient tests to conduct in comparison with uniaxial stretching, as information from this mode can yield information on many aspects of nonlinear stress-strain behaviors.[1-4] Ariano investigated the deformation of vulcanized rubber containing no compounding ingredients in the two principal stresses.[1] Film sample was clamped on the tensile testing machine and stretched simultaneously in two directions, perpendicular to one another in the same plane. This experiment is now known as biaxial tensile stretching. From the interpretation of stress-strain relationship compared with simple tension (uniaxial stretching), it was found that the addition of a transverse stress in biaxial stretching diminished the total maximum elongation attainable in the longitudinal direction. Urayama *et al*. reported the stretching behavior of vulcanized butadiene rubber in the neat and swelling states during biaxial stretching compared to uniaxial stretching, which was discussed using various models.[2] It was evident that the classical neo-Hookean model, which can explain the deformation behavior of uniaxial stretching, failed to reproduce the biaxial data. To understand biaxial stretching, the Ogden-type strain energy function with a single set parameter was satisfactory for explaining this nonlinear elastic behavior. This indicates the limitation of uniaxial data when attempting to determine the overall deformation behaviors of a material. Therefore, it is important to investigate the influence of biaxial stretching on the network and the domains of a SEBS sample in the bulk state, which represents the deformation behavior of the sample in actual use.

Investigation of change in microphase-separated structure is important to understand the deformation behaviors of block copolymers.[5-7] The mechanical stability of spherical PS domains, which are physical cross-linking points in SEBS, is a key point to investigate for improving the mechanical strength and toughness of SEBS. The orientation of the PEB chains during sample deformation is also crucial for understanding the mechanical properties of the material. *In situ* small-angle X-ray scattering (SAXS) and wide-angle X-ray scattering (WAXS) techniques are powerful methods to investigate the arrangement and deformation behavior of PS domains as well as the orientation state of the PEB chains. Many studies have reported on the deformation behavior of various types of thermoplastic elastomers based on these techniques.[8-18] Kawai *et al*. were the first researchers to publish about the deformation mechanism of block copolymers using simultaneous small-angle light scattering and SAXS measurements.[8] PS-*b*-polyisoprene (SI) and SIS with spherical PS domains as the linking points were uniaxially stretched. They concluded that the interdomain distance increased with increasing strain in the stretching direction, as observed from a change in the scattering intensity distribution from the SAXS results. Sakurai *et al*. investigated the quantitative deformation of PS domains containing different types of thermoplastic elastomers under uniaxial elongation using simultaneous SAXS measurements.[17] They clarified that the glassy domains deformed to prolate spheroids during uniaxial stretching. Suffering of PS domains was observed immediately upon stress application to the sample. The smaller the domains were, the larger the deformation. This refers to the dominance of stress concentration in the deformation of the glassy PS domains. As it was previously mentioned that additional mechanical deformation modes apart from uniaxial stretching are of interesting, we aimed to observe the deformation behavior of the material under equi-biaxial stretching compared to uniaxial stretching. In this study, the arrangement and deformation

behaviors of a microphase-separated structure in SEBS were investigated during uniaxial and equi-biaxial stretching using *in situ* SAXS measurements. Furthermore, the orientation of the soft segments was clarified using the WAXS technique.

2.2 Experiment

2.2.1 Sample preparation

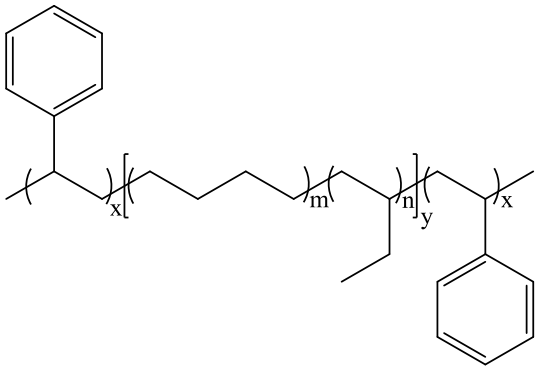

Figure 2.1. Chemical structure of the SEBS triblock copolymer.

A SEBS sample with 13 wt% PS was kindly provided by Asahi Kasei Chemical Co., Ltd, Japan. The chemical structure of SEBS is illustrated in Figure 2.1. The characteristics of the SEBS sample are specified in Table 1. SEBS pellets were dissolved in toluene and precipitated in methanol to remove impurities. Pieces of the sample were dried at room temperature and then under high-pressure vacuum until the weight stabilized. Purified samples were pressed into films at 150 °C without applying any pressure for 5 min, and then a pressure of 10 MPa was continuously applied for 1 min. Films were obtained with a thickness of 300-400 μm. To obtain the periodic structure of microphase separation, samples were annealed at 170 °C for 7 days in vacuo. The annealed films were quenched to room temperature when annealing was finished. Then, specimens were cut into a rectangular shape with dimensions of 5 × 30 mm^2 for the uniaxial test and 20 × 20 mm^2 for the equi-biaxial test. The PS content was determined

using proton nuclear magnetic resonance (^{1}H-NMR) spectroscopy. The ^{1}H-NMR (400 MHz) spectrum of SEBS was measured in $CDCl_3$ using a Bruker Avance-400 spectrometer. Number- and weight-averaged molecular weights of SEBS were determined through gel permeation chromatography. An HLC-8120GPC (TOSOH, CO.) system equipped with three columns was used with an RI-2031 plus refractive index detector. The eluent was tetrahydrofuran at a flow rate of 0.5 mL min^{-1}. Differential scanning calorimetry (DSC6220; SII NanoTechnology Inc.) was conducted from −100 to 150 °C at heating and cooling rates of 10 °C min^{-1} over the flow of nitrogen gas.

Table 2.1. Characteristics of SEBS

Sample	**PS content** (wt %)	$\bar{M}_n$[a]	$\bar{M}_w$[b]	**PDI**[c]	T_g **of PEB** (°C)	T_g **of PS** (°C)
SEBS	13	112,000	163,000	1.46	-45	50

[a]Number-averaged, [b]Weight-averaged molecular weights, and [c]Polydispersity index

2.2.2 *In situ* synchrotron radiation X-ray scattering measurement during simple stretching

For the uniaxial and equi-biaxial tests, each sample was clamped between the chuck grips of custom-built tensile testing machines (uniaxial machine: SENTECH Instrument GmbH; equi-biaxial machine: JUNKEN MEDICAL Co., Ltd), which were enabled for *in situ* measurement. Specimens were stretched at 1 mm s^{-1}. The synchrotron radiation X-ray scattering measurements were conducted with the BL05XU and BL40XU beamlines in the SPring-8 facility in Japan. Figure 2.2 shows schematic illustration of experimental set-up of *in situ* SAXS/WAXS measurements during uniaxial and equi-biaxial stretching. The beam size at the samples was 150×150 μm^2. The wavelength of the X-ray was 0.100 nm, and the sample-to-detector distance was 4 m for

SAXS and 0.1 m for WAXS. Samples were exposed to the X-ray beam for 0.4-1 s at ambient temperature. SAXS and WAXS patterns were taken with the beam perpendicular to the film surface (through view). 2D-scattering patterns of SAXS were obtained from a PILATUS 1M detector (DECTRIS Ltd) with a total pixel size of 172×172 μm^2, while WAXS 2D patterns were obtained from a PILATUS 1M detector for equi-biaxial testing and a flat panel detector with a total pixel size of 50 × 50 μm^2 for uniaxial testing. Data were converted from 2D patterns to 1D profile by integrating with FIT2D (ver. 16.041, Andy Hammersley/ESRF, Grenoble, France).

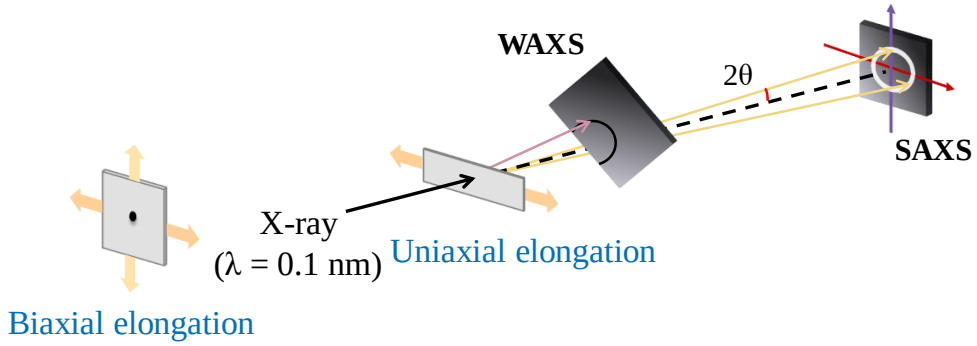

Figure 2.2. Schematic illustration of experimental set-up of *in situ* SAXS/WAXS measurements during uniaxial and equi-biaxial stretching.

2.3 Results and discussion

2.3.1 Stress-strain relationship

Figure 2.3 shows the stress-strain curve of SEBS during uniaxial and equi-biaxial stretching at 1 mm s^{-1}. The curves exhibited the typical S-shape for elastomeric materials. Uniaxial stretching showed a lower initial slope than equi-biaxial stretching. The initial moduli of uniaxial and biaxial stretching obtained by these initial slopes were 1.3 and 2.6 MPa, respectively. According to the linear elasticity theory, the initial moduli of uniaxial and equi-biaxial stretching correspond to $2G(1+\mu)$ and $2G(1+\mu)/(1-\mu)$, respectively, where μ is Poisson's ratio and G is the shear modulus. For incompressible

materials with μ = 1/2, the initial moduli become G and 2G for uniaxial and equi-biaxial stretching, respectively. Therefore, the results from the stress-strain curve were satisfactory, as they were related to the linear elasticity theory.[2] Uniaxial stretching exhibited smaller stress during stretching and finally showed larger tensile strength and strain at break than equi-biaxial stretching. The large strain at break of the uniaxial stretching seemed to be related to a conformational change in the PEB bridging segment from the *gauche* to the *trans* conformation during stretching.

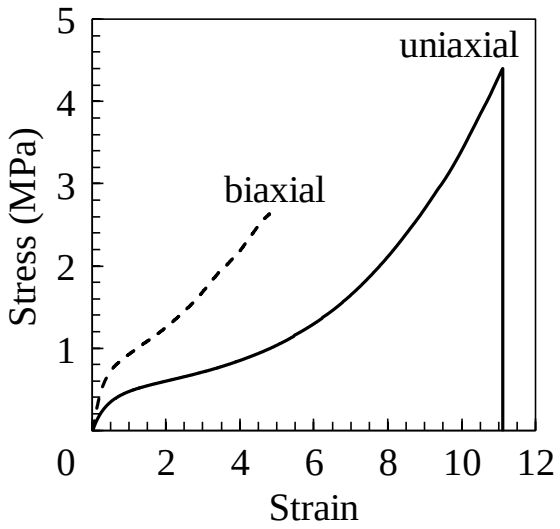

Figure 2.3. Stress-strain curve of SEBS samples during uniaxial and equi-biaxial stretching at 1 mm s^{-1} and 25 °C.

2.3.2 Structural characterization of SEBS

Figure 2.4 (a) and (b) shows the 2D SAXS pattern and 1D SAXS profiles of the SEBS film before and after annealing. Three sharp rings were observed in the scattering pattern of the annealed sample. As a ring-like pattern appeared instead of a spot pattern, the size of randomly oriented crystals was smaller than the beam size of X-ray. By conversion of the 2D pattern to the 1D profile along various directions, the three sharp rings transformed into three diffraction peaks. These crystalline peaks were observed at

scattering vectors (q) of 0.26, 0.36 and 0.45 nm^{-1}. These peak positions corresponded to the q relation of 1, √2 and √3, which can be assigned to the (110), (200) and (211) planes of the body-centered cubic (b.c.c.) lattice, respectively.[19] Fringes of intensity in the profile corresponded to the form factor, which indicates the shape and size of PS domains. The SEBS sample showed the characteristic of spherical domains. Numerical analysis was carried out to confirm the spherical PS domain characteristic and to determine the domain size. The calculation is discussed in section 2.3.4.

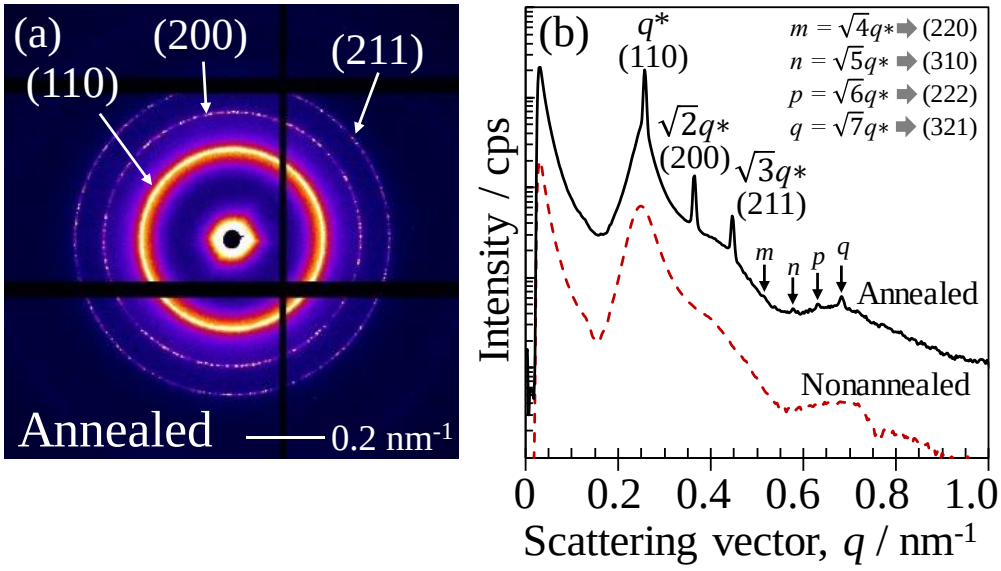

Figure 2.4. (a) 2D SAXS pattern of annealed SEBS at 170 °C for 7 days measured at 25 °C and (b) 1D SAXS profile of nonannealed and annealed SEBS.

Transmission electron microscope (TEM) was a complementary technique to confirm the microphase-separated structure of SEBS. Figure 2.5 shows two representative TEM micrographs of annealed SEBS taken at arbitrarily chosen directions of microtoming of a bulk sample. Dark circular morphology refers to the PS domains, caused by the RuO_4 staining, and the PEB matrix is bright. Well-ordering of spherical PS domains was observed from the TEM micrographs.

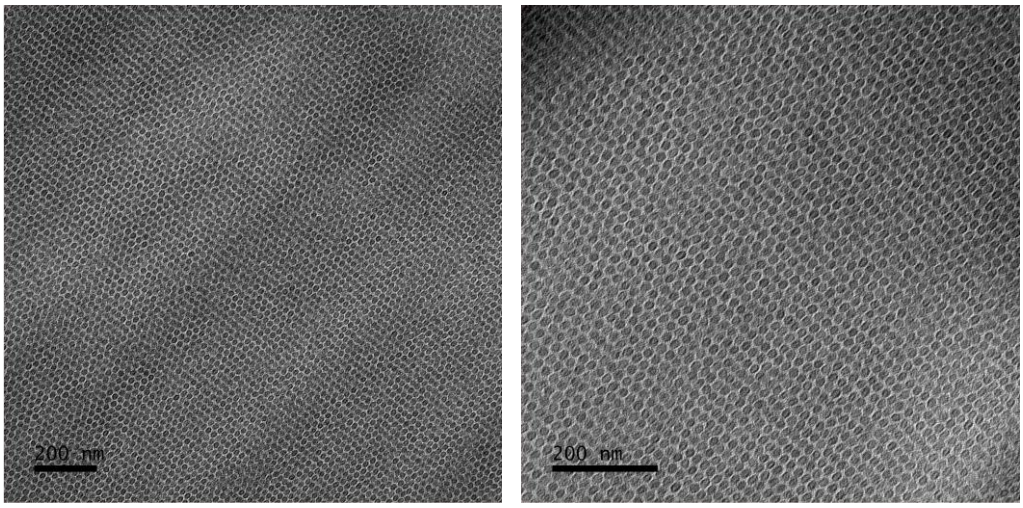

Figure 2.5. Two typical TEM micrographs of ultrathin sections of SEBS bulk sample. The PS domains appear dark caused by the RuO_4 staining.

2.3.3 Changes in microphase-separated structure of SEBS

Figures 2.6 and 2.7 show the 2D SAXS patterns and 1D SAXS profiles of SEBS during uniaxial and equi-biaxial stretching, respectively. 2D SAXS pattern at the strain of 2.5 during equi-biaxial stretching was magnified and its contrast was changed for clarity. The magnified 1D SAXS profiles at low *q* region in the X-axis and Y-axis of SEBS during equi-biaxial stretching are shown in Figure 2A.4 in the Appendix. For uniaxial stretching, the sample was stretched in a horizontal direction. Data analyzed from the stretching and transverse directions during uniaxial stretching as well as in the X- and Y-axis directions during biaxial stretching are shown in the 1D SAXS profiles in Figures 2.6 (b) and (c) and 2.7 (b) and (c), respectively. Three diffraction peaks clearly shifted to a lower *q* region in the stretching direction, while they shifted toward a higher *q* region in the transverse direction. On the other hand, the diffraction peaks shifted to

the lower q region in both the X- and Y-axis directions during equi-biaxial stretching. These shifts referred to a change in the plane spacing (d) during stretching, and can be converted through $d = 2\pi/q$. During uniaxial stretching, all plane spacings increased with increasing strain in the stretching direction, while they decreased in the transverse direction. For equi-biaxial stretching, all plane spacings increased isotropically with increasing strain in both stretching axes. From the 2D pattern, the ring pattern contained dot-like and line-like characteristics when the sample was stretched. These phenomena could be explained based on the calculation of the 2D pattern *via* the fast Fourier transform (FFT) of the (110) plane of the b.c.c. lattice. The calculated patterns are shown in the Appendix (Figures 2A.1 to 2A.3). Scattering patterns are related to the characteristic features of reflection planes of the paracrystalline lattice.[20] In the case that the size of grain is much larger than beam size, a dot-like pattern is observed. In contrast, a line-like pattern emerges when the size of grain is smaller. In the random-oriented multigrain structure of SEBS, it is feasible that different sizes of reflection planes occurred, resulting in the combination of two types of patterns. Furthermore, a four-point smeared pattern appeared in the 2D SAXS pattern during uniaxial stretching from strain 2 until the sample was broken. This might indicate that some PS domains were fractured upon stretching.[21] Streaks were observed in the 2D pattern during equi-biaxial stretching. This refers to the possibility of voids on the mesoscopic scale that occurred during isotropic stretching.

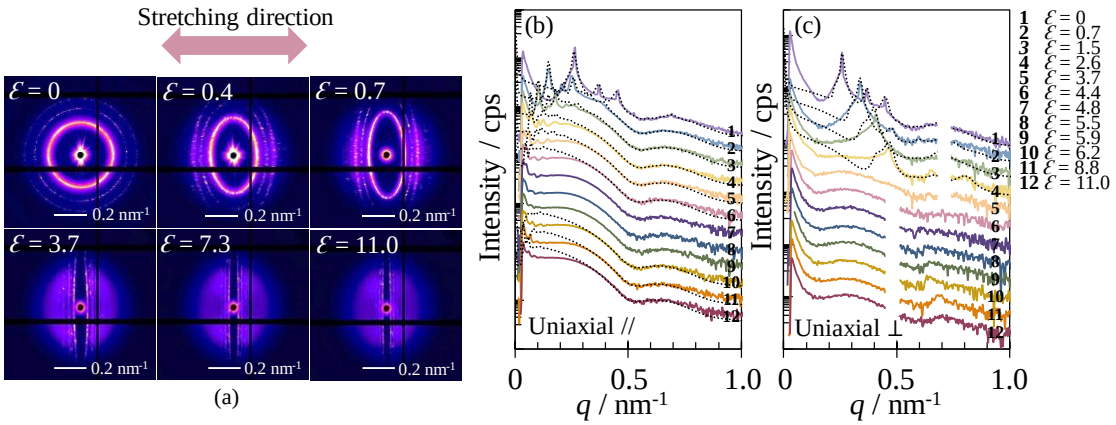

Figure 2.6. (a) 2D SAXS patterns of SEBS during uniaxial stretching at 1 mm s^{-1} and 25 °C at various strains with the beam perpendicular to the film surface (through view). (b) 1D SAXS profiles obtained from (a) in the stretching direction and (c) transverse direction. Black dot lines were obtained from the model calculation.

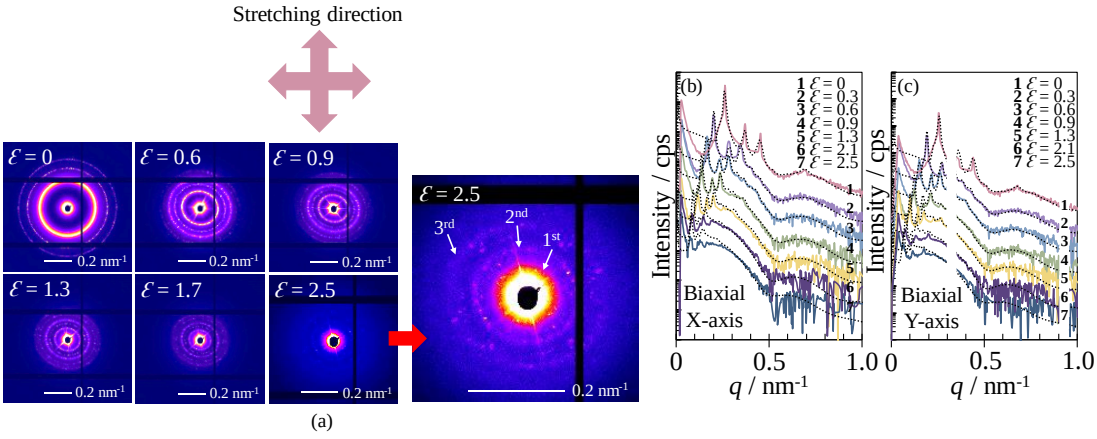

Figure 2.7. (a) 2D SAXS patterns of SEBS during equi-biaxial stretching at 1 mm s^{-1} and 25 °C at various strains with the beam perpendicular to the film surface (through view). (b) 1D SAXS profiles obtained from (a) in the X-axis and (c) Y-axis. Black dot lines were obtained from the model calculation.

2.3.4 Model calculation

Form factors and structure factors that appeared in the 1D SAXS profiles were simulated by varying important factors to obtain the fitted results. The equations used in the numerical calculation are explained below. All equations were written using the scipy library in Python version 3.7 and then submitted for calculation in the supercomputer system ITO, Kyushu University. The radius of spherical PS domains and the length of the semiaxes of prolate and oblate spheroid PS domains were obtained from the form factor. Variance, which indicates the polydispersity of the domain length, was examined based on the Gaussian distribution. Full width at half maximum (FWHM) was determined from the width of the 3rd diffraction peak ($d_{(211)}$) at its half maximum intensity in order to discuss about an ordering of PS domains.

The model calculation was applied to observe the deformation of PS domains and the packing regularity of the lattice. Solid lines fitted in 1D SAXS profiles in Figures 2.6 (b) and (c) and 2.7 (b) and (c) were obtained from the model calculation. These I-q profiles are the combination between the structure factor, $Z(q)$, and the form factor, $f(q)$. Thus, the intensity from both factors must be considered and is included in equation (2.1).

$$I(q) \propto \langle f^2(q) \rangle - \langle f(q) \rangle^2 + \langle f(q) \rangle^2 Z(q) \qquad (2.1)$$

where $\langle f^2(q) \rangle$ and $\langle f(q) \rangle^2$ denote an average function of the form factor, f(q), and Z(q) refers to the structure factor (lattice factor) function. Here, an average function of the form factor was applied, as different size distributions of the PS domain were proposed.[17, 19, 22-23] To discuss the shape of the PS domain, the form factor was considered dominant. In the initial state, the spherical form factor, $f(q)_{sph}$, was used.

$$f(q)_{sph} = 3V \frac{sinqR - qRcosqR}{(qR)^3} \qquad (2.2)$$

where the volume of the domain with radius R is $V = \frac{4}{3}\pi R^3$. During mechanical deformation, the domain was assumed to deform to prolate spheroids during uniaxial

elongation and to oblate spheroids during equi-biaxial elongation. The form factor function of both particles was formulated as:

$$f(q, \nu, R_a, \phi, \mu) = 3V \frac{sinU - UcosU}{U^3} \quad (2.3)$$

where the volume of the spheroid is $V = \frac{4}{3}\pi {R_a}^3 \nu$. As spheroids have two different dimensions, the axial ratio, $\nu = \frac{R_b}{R_a}$, must be considered ($\nu > 1$ for prolate spheroids and $\nu < 1$ for oblate spheroids). R_a is defined as the length of the semiminor axis (α), which lies in the x-y plane, while R_b is the length of the semimajor axis (γ), which lies in the YZ plane. The dimensions of the prolate and oblate spheroids are shown in Figure 2.8. The longer and shorter lengths of the semi-axes of both spheroids are proposed to be parallel and perpendicular to the stretching direction, respectively.

For the form factor in the YZ-plane, U_b was formulated as:

$$U_b(q, \nu, R_a, \phi) = qR_a\sqrt{\sin^2\phi + \nu^2\cos^2\phi} \quad (2.4)$$

For the form factor in the XY-plane, U_a was formulated as:

$$U_a(q, \nu, R_a, \phi, \mu) = qR_a\sqrt{\sqrt{1 - \sin^2\phi\cos^2\mu} + \nu^2\sin^2\phi\cos^2\mu} \quad (2.5)$$

The polar angles, ϕ and μ, were assumed to be zero, as the alignment of the PS domain was expected to be parallel to the axis during deformation. Additionally, the Gaussian distribution function was used since the polydispersity of the radius was considered:

$$f(R) = \frac{1}{\sqrt{2\pi\sigma^2}} e^{-\frac{(R-\bar{R})^2}{2\sigma^2}} \quad (2.6)$$

where $\bar{R}$ is the average length of the semi-axis of the PS domain and σ^2 is the variance of R. The Gaussian function was normalized ($\int_0^\infty f(R)dR = 1$) and included in the calculation of $\langle f^2(q)\rangle$ and $\langle f(q)\rangle^2$. In the system without a size distribution, the assumption of $\langle f^2(q)\rangle = \langle f(q)\rangle^2$ can be made.[24] However, a polydisperse system was

applied for the SEBS sample. Thus, $\langle f^2(q)\rangle$ and $\langle f(q)\rangle^2$ were calculated according to equations (7) and (8), respectively:

$$\langle f^2(q)\rangle = \int_0^\infty |f(q)|^2 f(R) dR \tag{2.7}$$

$$\langle f(q)\rangle^2 = (\int_0^\infty f(q) f(R) dR)^2 \tag{2.8}$$

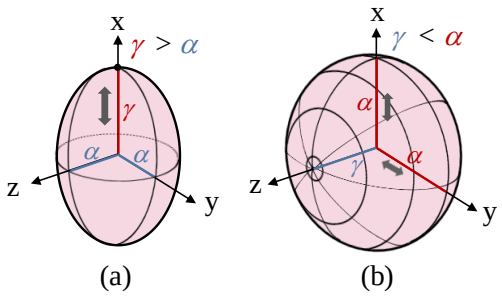

Figure 2.8. Schematic illustration of deformed PS domains: (a) prolate and (b) oblate spheroids.

For Z(q), the calculation was performed according to the paracrystal theory.[24-25] The calculation was performed from the following equation:

$$\overrightarrow{a_1} \cdot \vec{q} = \frac{1}{2} qa(sin\theta cos\phi + sin\theta sin\phi + cos\theta) \tag{2.9}$$

$$\overrightarrow{a_2} \cdot \vec{q} = \frac{1}{2} qa(-sin\theta cos\phi - sin\theta sin\phi + cos\theta) \tag{2.10}$$

$$\overrightarrow{a_3} \cdot \vec{q} = \frac{1}{2} qa(-sin\theta cos\phi + sin\theta sin\phi - cos\theta) \tag{2.11}$$

$$|F_k(q)| = exp\left[-\frac{1}{8}\Delta a^2 q^2[(sin\theta cos\phi + sin\theta sin\phi + cos\theta)^2 + (-sin\theta cos\phi - sin\theta sin\phi + cos\theta)^2 + (-sin\theta cos\phi + sin\theta sin\phi - cos\theta)^2)]\right] \tag{2. 12}$$

$$Z_k = \frac{1-|F_k(q)|^2}{1-2|F_k(q)|\cos(\overrightarrow{a_k}\cdot\vec{q})+|F_k(q)|^2} \tag{2.13}$$

$$Z(q) = \frac{1}{4\pi}\int_0^{2\pi} d\phi \int_0^{\pi} d\theta \, Z_1 Z_2 Z_3 \, sin\theta \tag{2.14}$$

where Δa is the distortion of the lattice point from the ideal lattice point and a is the length of the lattice. In this work, a was calculated from the spacing of the (110) plane

of the b.c.c. lattice because the crystalline peak of the (110) plane showed the highest intensity.

2.3.5 Deformation of PS domains

Form factor results were investigated for considering the deformation of PS domains as the fringes of intensity that shifted during sample stretching. The calculation method was explained in section 2.3.4. From the SAXS results shown in Figure 2.6 (b) and (c), the form factor shifted to the lower q region in the stretching direction, while it shifted to the higher q region in the transverse direction during uniaxial stretching. The characteristics of the form factor along the stretching and transverse directions were different in the uniaxial stretching mode. Therefore, spherical PS domains were confirmed to transform into prolate spheroids. On the other hand, the form factor shifted toward the lower q region in both the X- and Y-axis directions during equi-biaxial stretching, as shown in the SAXS results in Figure 2.7 (b) and (c). This shift indicated isotropic deformation along the two axes of the stretching directions, verifying the transformation of spherical PS domains to oblate spheroids during equi-biaxial stretching. The semimajor axis (γ) of the prolate spheroid shown in Figure 2.8 was parallel to the stretching direction under uniaxial stretching, while the semiminor axis (α) of the oblate spheroid was parallel to the stretching direction under equi-biaxial stretching. Figure 2.9 (c) shows the average length of the semiaxes of the PS domains during uniaxial stretching, and Figure 2.10 (b) shows the average length of the semimajor axes of the PS domain during equi-biaxial stretching. It was found that the average radius of spherical PS domains in the initial state was 7.9 nm. When the sample was uniaxially stretched, the average length of the semimajor axis of the PS domains increased, while the average length of the semiminor axis decreased with increasing strain. SEBS is a

material with Poisson's ratio of 0.49. It was considered an incompressible material. Therefore, constant volume of PS domains was assumed for calculating semimajor axis of the oblate spheroid. The average length of the semiminor axis of an oblate spheroid increased equally in both stretching directions, while the semimajor axis decreased with increasing strain. These results indicated the transformation of PS domains when the sample was stretched during both stretching modes. Discussion about the degree of deformation of the spheroids has been done with the discussion of an arrangement of PS domains in section 2.3.6.

2.3.6 Arrangement of PS domains

The relationship of strain calculated from plane spacing ($\Delta d/d_0$) and real strain was compared to affine deformation. $\Delta d/d_0$ is the deformation on the mesostructural scale, while film strain (real strain) is the deformation on the macroscopic scale. The real strain was calculated from the real deformation of the film sample, which was observed from the deformation of the lattice pattern stamped on the film. Figure 2.9 shows the relationship of real strain and $\Delta d/d_0$ during the uniaxial stretching test in the (a) stretching and (b) transverse directions. Figure 2.10 (a) shows the relationship of real strain and $\Delta d/d_0$ obtained from the biaxial stretching test. The diagonal lines shown in Figures 2.9 and 2.10 correspond to affine deformation. SEBS showed affine deformation up to strain 4.4 for uniaxial stretching and strain 1.3 for equi-biaxial stretching. The strain at which deviation from the affine deformation occurred is defined as $\mathcal{E}_{\text{d-A}}$. Below $\mathcal{E}_{\text{d-A}}$, simple arrangement of PS domains occurred because geometrical restriction, such as contacting PS domains and extending to a maximum length of PEB chains, did not occur. The (110), (200) and (211) planes in the stretching direction of both extension modes exhibited the same trend to follow the affine deformation. A simple arrangement of PS domains and

linking of the PEB bridging chains could be factors of the plane-independent phenomenon. The number of PEB chains that link PS domains in each plane might be equivalent, leading to an equal increase in the spacing of each plane. Above $\mathcal{E}_{\text{d-A}}$, since PS domains in the transverse direction started to come into contact with each other[26] and the distance between PS domain surfaces reached the maximum length of PEB chains in the full-stretched state, it seemed that irreversible phenomena, such as the breaking of PS domains, pulling out of PEB chains from PS end blocks, breaking PEB chains, and so on, started to occur. Changes in the irreversible structure were confirmed by the combination between cyclic tensile testing and SAXS measurement. The details will be explained in Chapter 3. Schematic illustration of an arrangement of PS domain during uniaxial and equi-biaxial stretching are shown in Figure 2.15, and Figure 2.16, respectively. During the equi-biaxial mode, simultaneous stretching in two directions led geometrical restriction of the SEBS sample as well as irreversible phenomena at a smaller strain than for the uniaxial stretching, which resulted in a lower $\mathcal{E}_{\text{d-A}}$ for the biaxial mode than for the uniaxial stretching mode. For an increase in the spacing of each plane, uniaxial stretching still showed the plane-independent phenomenon, while biaxial stretching did not. This difference between the two stretching modes highlighted their different deformation behaviors above $\mathcal{E}_{\text{d-A}}$. PS domains had more freedom to arrange themselves during uniaxial stretching than during equi-biaxial stretching. Therefore, all planes could deform equally during uniaxial stretching because the structure was stretched in only one direction. In contrast, restriction of the arrangement of PS domains occurred during equi-biaxial stretching, causing unequal deformation of each plane. Figures 2.9 (c) and 2.10 (b) illustrate an average length of the semiaxes of ellipsoidal PS domains with increasing real strain during uniaxial and biaxial stretching, respectively. For the uniaxial stretching mode, the semimajor axis of the prolate spheroid slightly increased, while the

semiminor axis slightly decreased above $\mathcal{E}_{d\text{-}A}$. Additionally, the semiminor axes of the oblate spheroid slightly increased above $\mathcal{E}_{d\text{-}A}$. This slight deformation of the domains illustrated the effect of the irreversible phenomena on the deformation of PS domains.

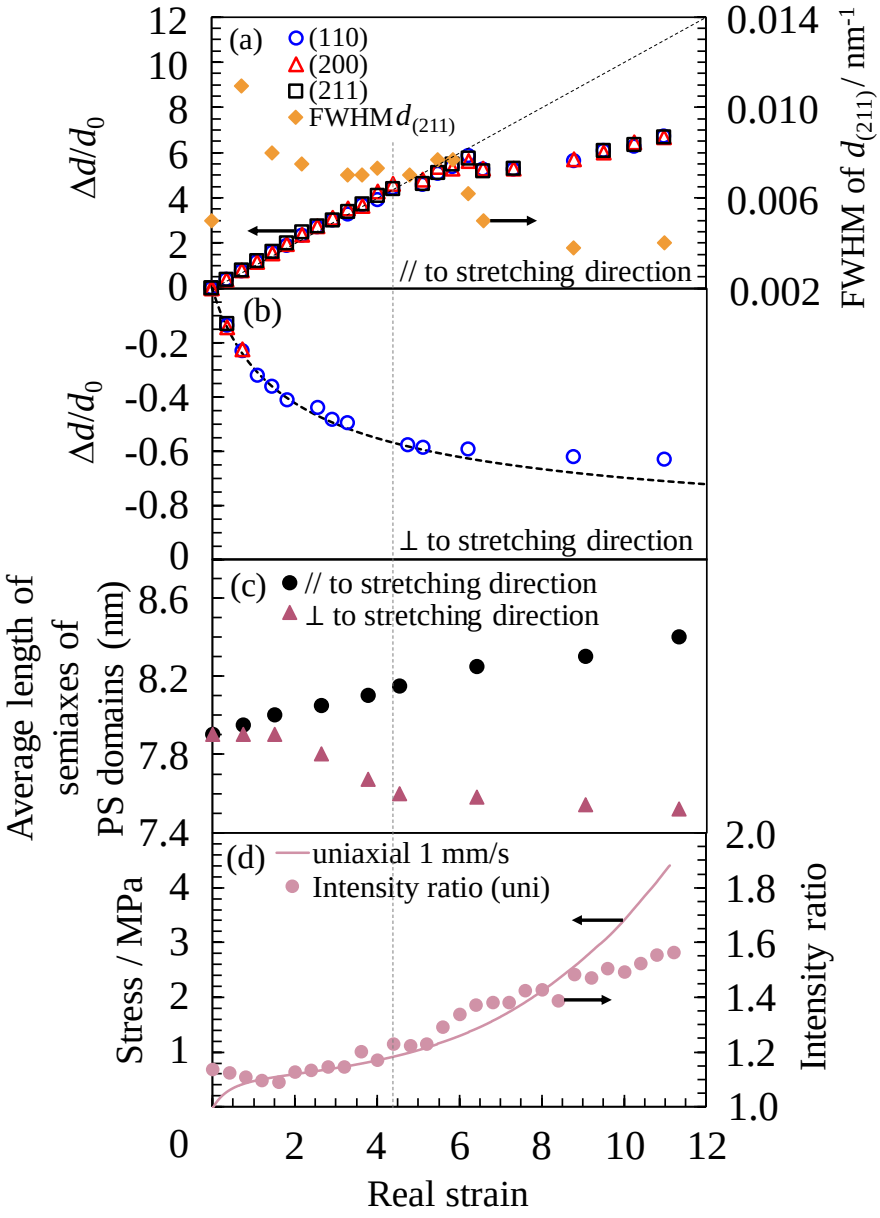

Figure 2.9. Deformation behaviors of SEBS during uniaxial stretching at 1 mm s^{-1}. (a) Relationship between real strain and $\Delta d/d_0$ in the stretching direction and the FWHM of $d_{(211)}$. (b) Relationship between real strain and $\Delta d/d_0$ in the transverse direction. (c) Average length of semiaxes of PS domains. (d) Relationship between real strain and the intensity ratio as well as the stress-strain curve of SEBS.

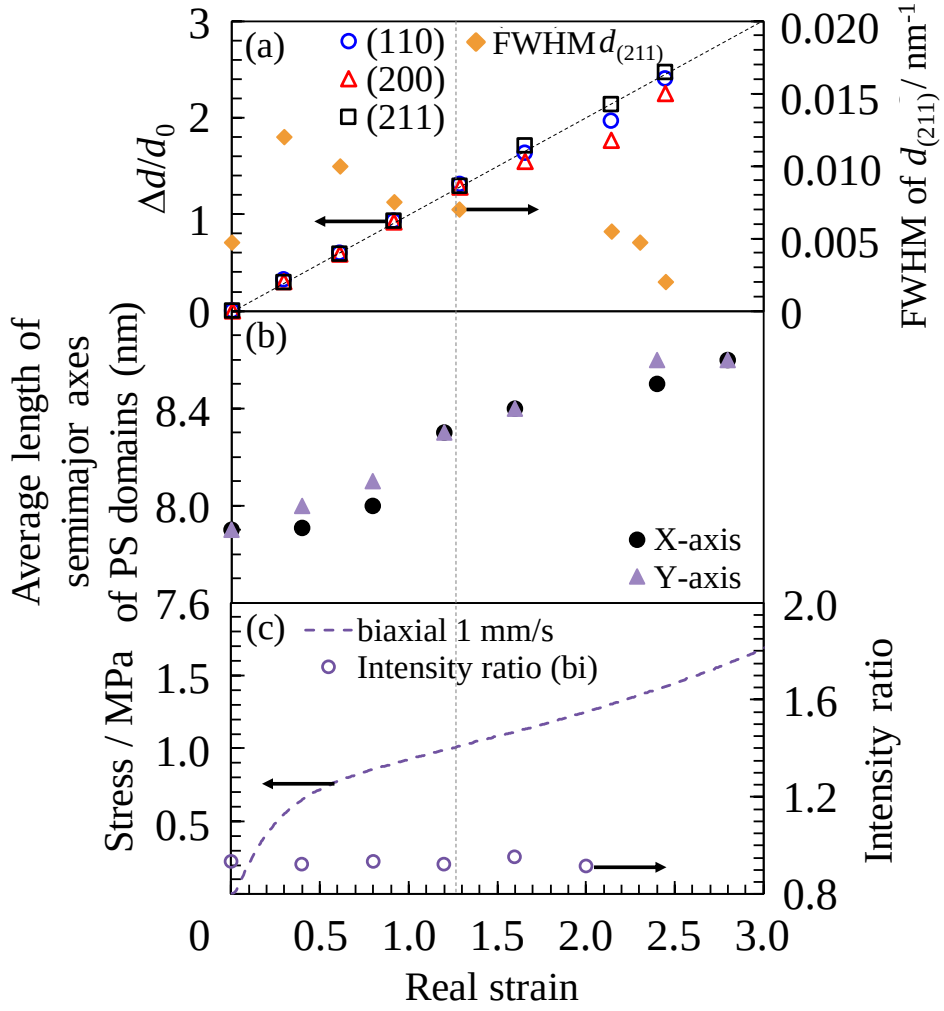

Figure 2.10. Deformation behaviors of SEBS during equi-biaxial stretching at 1 mm s^{-1}. (a) Relationship between real strain and $\Delta d/d_0$ in the stretching direction and the FWHM of $d_{(211)}$. (b) Average length of the semimajor axes of PS domains. (c) Relationship between real strain and the intensity ratio as well as the stress-strain curve of SEBS.

2.3.7 Orientation of PEB soft chains

Figures 2.11 (a) and (b) show the 2D WAXS patterns and 1D WAXS profiles of SEBS during uniaxial stretching, respectively. Figures 2.12 (a) and (b) show q-range and azimuthal angle (ϕ) as well as azimuthal plot of WAXS results during uniaxial stretching, respectively. The 2D WAXS patterns and 1D WAXS profiles as well as analyzed region

of *q*-range and ϕ of SEBS during equi-biaxial stretching are shown in the Figure 2.13 and Figure 2A.5 in the Appendix. *In situ* WAXS measurement is an effective technique for confirming the orientation phenomenon.[14, 27] In SEBS, the PEB chains is expected to be oriented in the stretching direction upon uniaxial stretching. It was reported that orientation in SEBS can occur under selective conditions, depending on the fraction of ethylene and butylene segments in the PEB midblock.[28-29] From the WAXS results in Figures 2.11 and 2.13, the position of the amorphous halo did not shift, and a new crystalline peak did not occur with increasing strain in either stretching mode. This suggested the lack of a highly oriented structure of the molecular chains. The molar fraction of ethylene and butylene units in the PEB chains, which affects the orientation of the polymer chain, was calculated based on the number of protons in NMR measurements. The fraction of ethylene units was estimated to be two because the midsegment of the precursor polymer consisted of 1,4- and 1,2-additions of butadiene that affords 1,4-butylene (two ethylenes) and 1,2-butylene units by hydrogenation. As a result, the fraction was estimated to be ethylene:butylene = 0.27:0.73. The lower content of ethylene units than butylene units led to a lower orientation ability of the PEB chains. To analyze the orientation of the soft segment more quantitatively, the intensity ratio was calculated from the peak intensity of the amorphous halo in the meridional and horizontal directions. Figure 2.12 and 2A.5 in the Appendix shows the *q*-range and azimuthal angle (ϕ) of the WAXS results during uniaxial and equi-biaxial stretching, which were used to calculate the intensity ratio. Figures 2.9 (d) and 2.10 (c) show the intensity ratio obtained from the WAXS results during uniaxial and biaxial stretching, respectively, in two directions. This ratio was expected to remain constant in the case of no orientation. There was a slight increase in the ratio during uniaxial elongation from strain 4, indicating that orientation of the PEB chains occurred. This orientation could occur during uniaxial

stretching; however, a highly-oriented structure could not be formed because of a higher fraction of the butylene segment than of the ethylene segment in the PEB midblock. On the other hand, the ratio remained unchanged during equi-biaxial stretching, indicating no orientation of the PEB chains. Simultaneous stretching in two directions made orientation impossible.

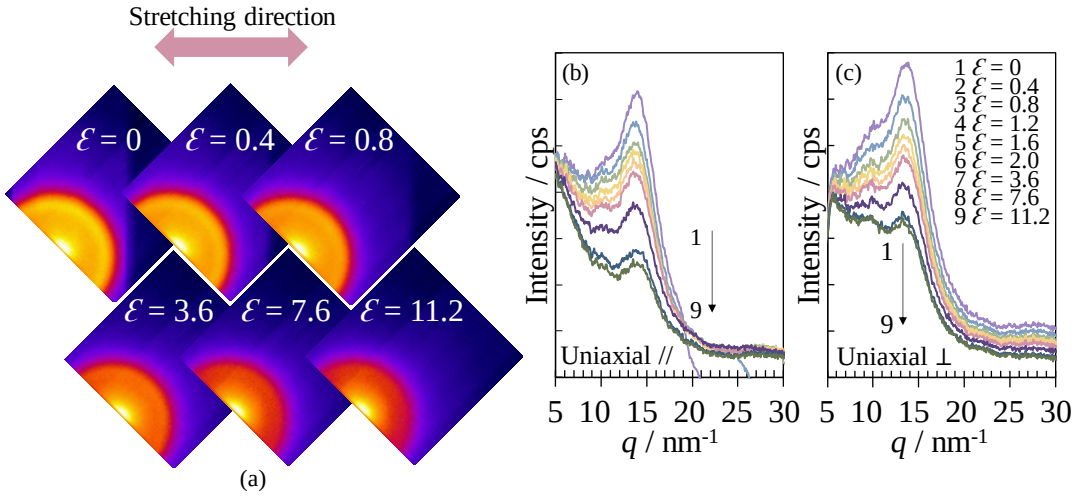

Figure 2.11. (a) 2D WAXS patterns of SEBS during uniaxial stretching at 1 mm s^{-1} and 25 °C at various strains with the beam perpendicular to the film surface (through view). (b) 1D WAXS profiles obtained from (a) in the stretching direction and (c) transverse direction.

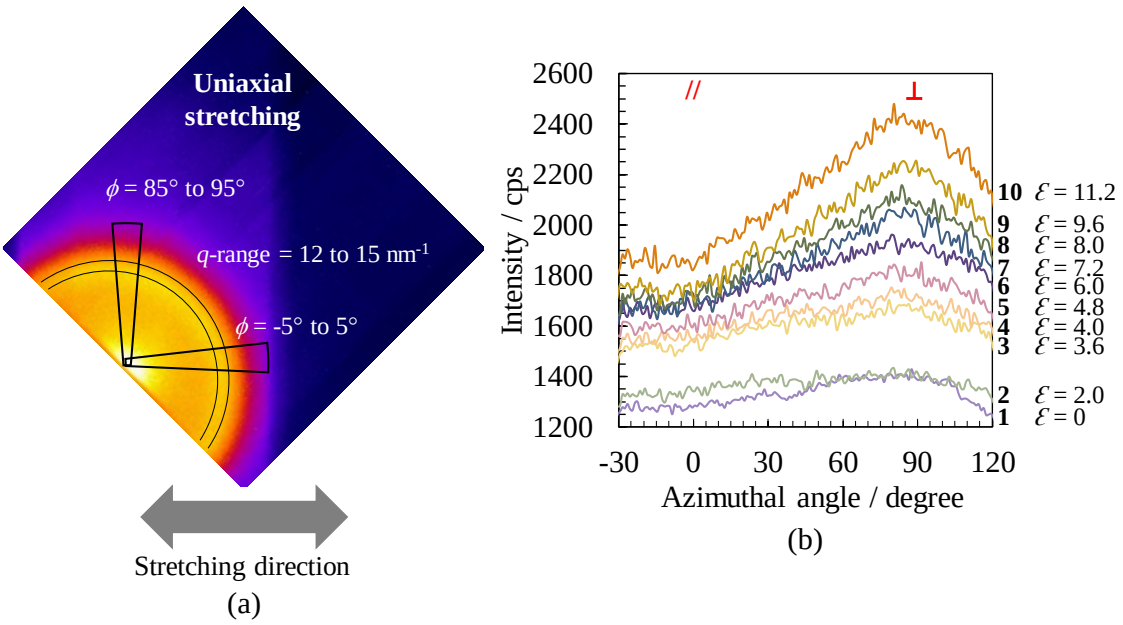

Figure 2.12. (a) q-range and azimuthal angle (ϕ) (b) Azimuthal plot of WAXS results during uniaxial stretching at 1 mm s^{-1} and 25 °C at various strains with the beam perpendicular to the film surface (through view).

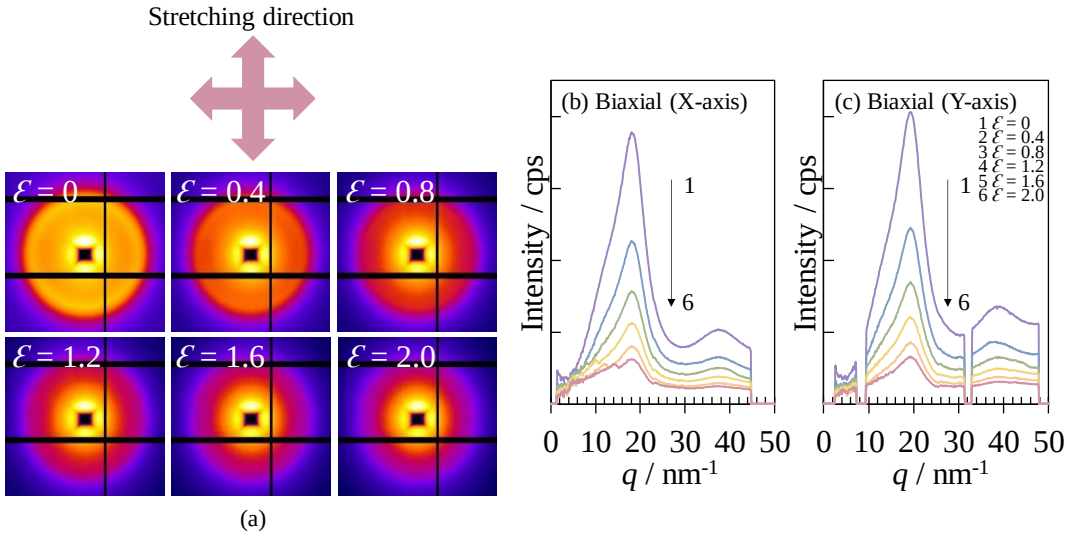

Figure 2.13. (a) 2D WAXS patterns of SEBS during equi-biaxial stretching at 1 mm s^{-1} and 25 °C at various strains with the beam perpendicular to the film surface (through view). (b) 1D WAXS profiles obtained from (a) in the X-axis and (c) Y-axis.

2.3.8 Ordering transition of PS domains

Changes in FWHM in Figure 2.9 (a) and 2.10 (a) as well as the 1D SAXS profiles and 2D SAXS patterns shown in Figure 2.6 were focused on discussing a change in the ordering of PS domains above $\mathcal{E}_{\text{d-A}}$. The values of FWHM was obtained from the 3$^{\text{rd}}$ diffraction peak ($d_{(211)}$). A decrease in FWHM reflects an increase in the ordering. For both uniaxial and equi-biaxial stretching, the FWHM increased upon stretching, indicating a decrease in ordering of PS domains. Interestingly, the FWHM suddenly decreased at a strain of 6.2 during uniaxial stretching and at strain 2.3 during equi-biaxial stretching, indicating a sudden increase in ordering of PS domains. Figure 2.14 (a) 2D SAXS patterns and (b) 1D SAXS profiles of SEBS upon uniaxial stretching at strains of 5.9 and 6.2. In the stretching direction, the width of the diffraction peaks increased from the initial state, which was consistent with the result of FWHM. These results indicated a decrease in lattice ordering. Interestingly, the diffraction peak suddenly became sharper at a strain of 6.2. This change in the width in the profile may correspond to the possibility of transition of the lattice ordering during deformation. On the contrary, in the transverse direction, intensity of diffraction peak gradually decreased and increased again. It seems that the change from strain 5.9 and 6.2 is discontinuous. Therefore, at strain around 6, the locked state emerged by contacts of PS domains and extended PEB chains. The transition to the higher order structure occurred by releasing locked state. Figures 2.15 (a) and (b) illustrate a schematic of the arrangement of the PS domains in the (110) and (200) planes observed from the top view of the original b.c.c. lattice during uniaxial stretching. The black line represents an alignment of the diffraction plane. The plane spacings of the (110) and (200) planes and the semiminor axis (α) of the PS domains in the transverse direction were calculated with increasing strain. It was found that the domains in the (200) plane started to come into contact with each other at a strain of 4.

This contact brought about changes in the ordering and deformation behavior of the lattice. The effect of domain contact became predominant when the PS domains in the (110) plane moved closer. At a strain of 5.9, the semiminor axis (α) of the PS domains was 7.6 nm with a plane spacing of 9.3 nm. Since the (200) plane already had domains that came into contact with each other, and ordering of the lattice became lower, some PS domains in the (110) plane might have come into contact with adjacent domains in this state. This contact was inferred as a factor that rearranged the PS domains, resulting in the reordering of PS domains. The sudden change in the scattering pattern and FWHM which indicate the ordering transition of PS domains was also observed during equi-biaxial stretching at the strain. Schematic illustration of the arrangement of the PS domains during equi-biaxial stretching is shown in Figure 2.16.

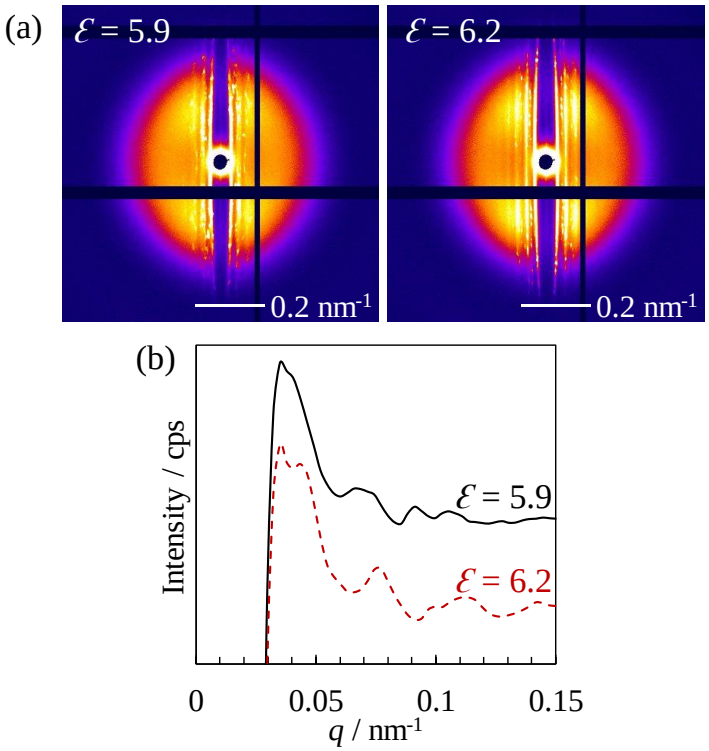

Figure 2.14. (a) 2D SAXS patterns and (b) 1D SAXS profiles of SEBS upon uniaxial stretching at strains of 5.9 and 6.2.

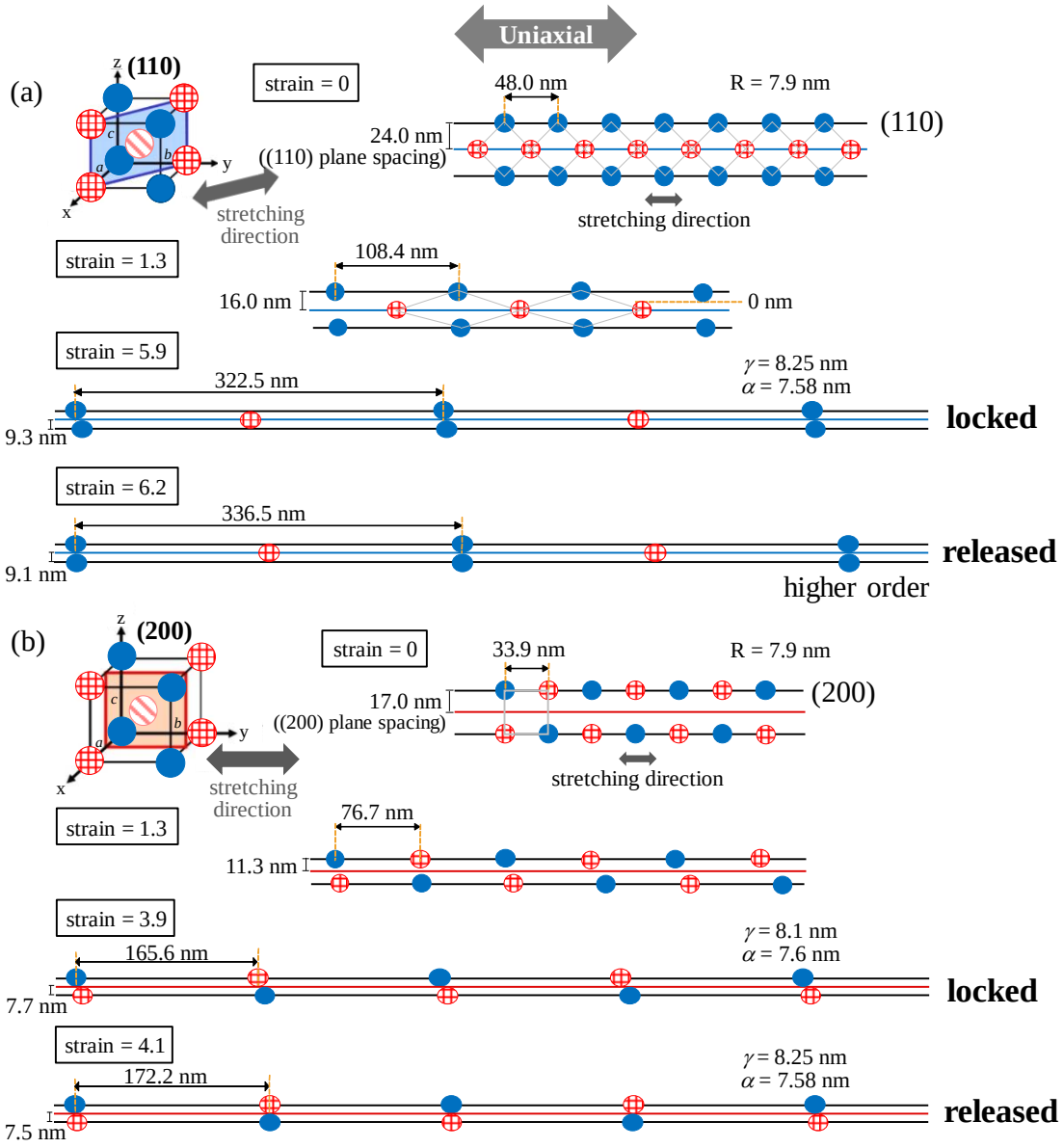

Figure 2.15. Schematic illustration of an arrangement of PS domains in the (a) (110) and (b) (200) planes during uniaxial stretching.

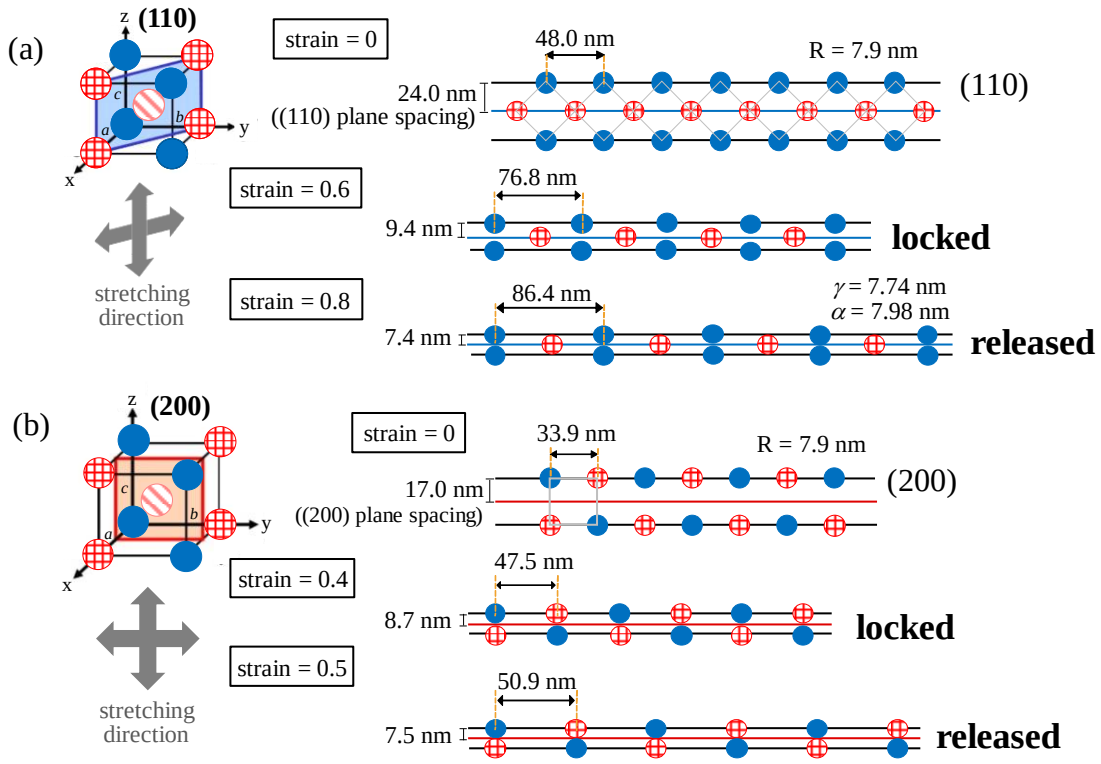

Figure 2.16. Schematic illustration of an arrangement of PS domains in the (a) (110) and (b) (200) planes during uniaxial stretching.

2.4 Conclusions

In situ synchrotron radiation SAXS/WAXS measurements revealed a change in the microphase-separated structure of SEBS during uniaxial and equi-biaxial deformation. WAXS measurements revealed the orientation of the PEB chains during uniaxial stretching only at high strain region. In contrast, no orientation was found during equi-biaxial stretching. From SAXS results, spherical PS domains transformed to prolate spheroids during uniaxial stretching and to oblate spheroids during equi-biaxial stretching. Both deformation modes similarly followed the affine deformation up to $\mathcal{E}_{\text{d-A}}$ due to the simple arrangement of PS domains and the extension of PEB chains. Ordering of PS domain decreased upon stretching. Above $\mathcal{E}_{\text{d-A}}$, PS domains came into contact with each other in the transverse direction, and the distance between PS domains reached the

maximum length of PEB chains in the fully-extended state, leading to irreversible phenomena in the sample. The plane-independent phenomenon was still occur during uniaxial stretching, however, equi-biaxial stretching showed plane-dependent phenomenon. Equi-biaxial stretching showed a lower $\varepsilon_{d\text{-}A}$ than uniaxial stretching due to entanglement effect of PEB chains. After contact of PS domains, ordering suddenly increased at around strain 6 and 2 during uniaxial and equi-biaxial stretching, respectively, due to the release of locked state of PS domains and extended PEB chains. This is explained based on the sudden change in FWHM of the (211) diffraction peak and shift to smaller plane spacing.

Appendix

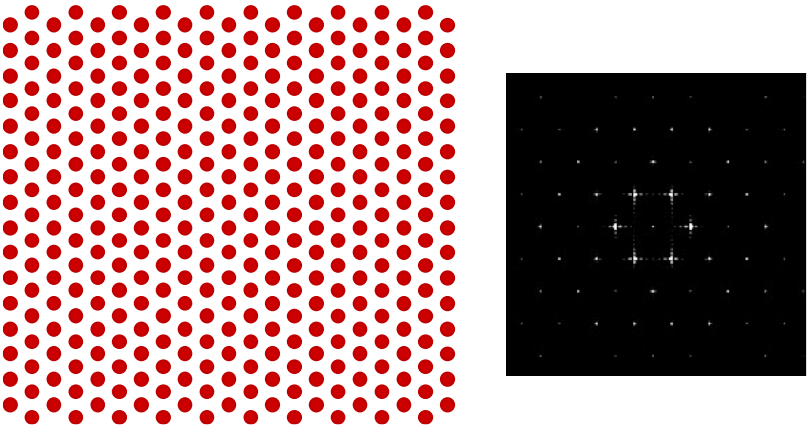

Figure 2A.1. Calculation of the 2D pattern of the (110) plane of the b.c.c. lattice at initial state *via* the FFT.

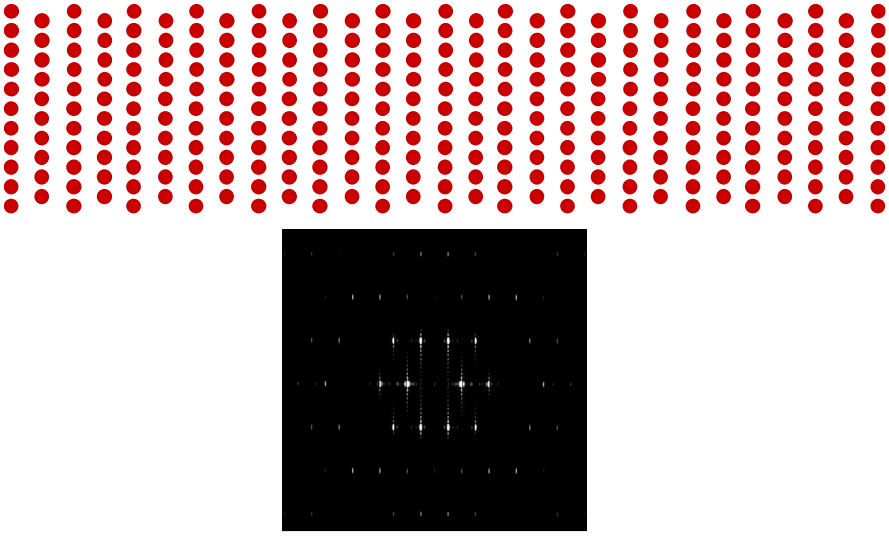

Figure 2A.2. Calculation of the 2D pattern of the (110) plane of the b.c.c. lattice in the case that the size of grain is much larger than beam size *via* the FFT. (dot-like pattern)

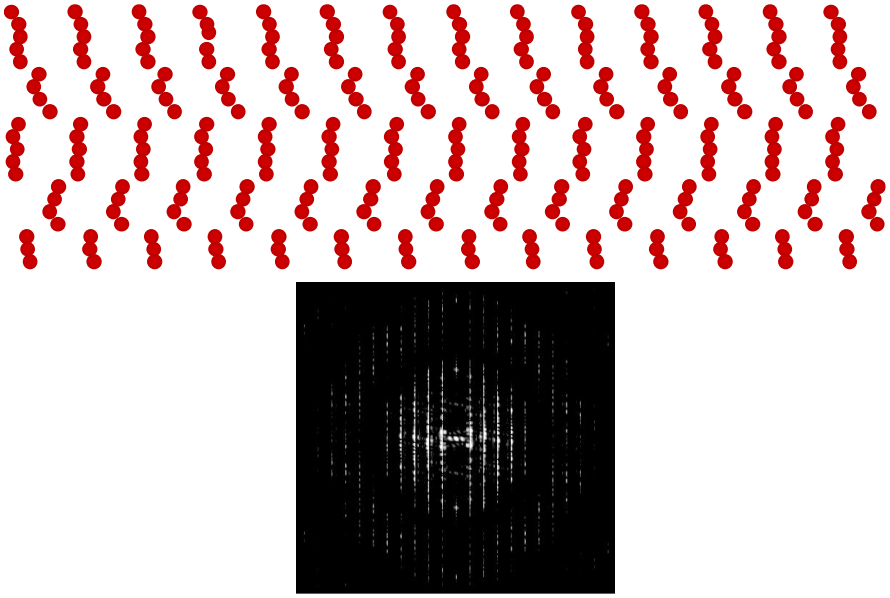

Figure 2A.3. Calculation of the 2D pattern of the (110) plane of the b.c.c. lattice in the case that the size of grain is much smaller than beam size *via* the FFT. (line-like pattern)

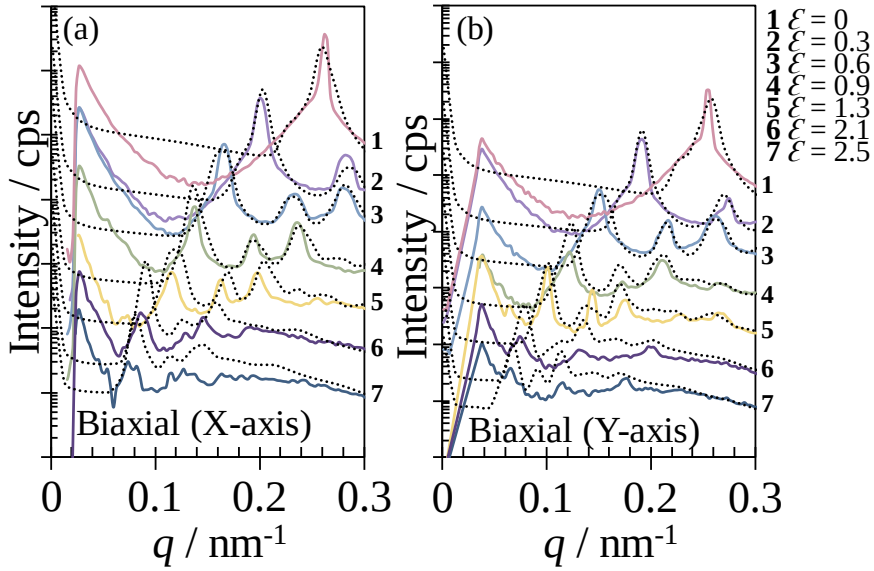

Figure 2A.4. Magnified 1D SAXS profiles in (a) the X-axis and (b) Y-axis of SEBS during equi-biaxial stretching at 1 mm s^{-1} and 25 °C at various strains with the beam perpendicular to the film surface (through view). Black dot lines were obtained from the model calculation.

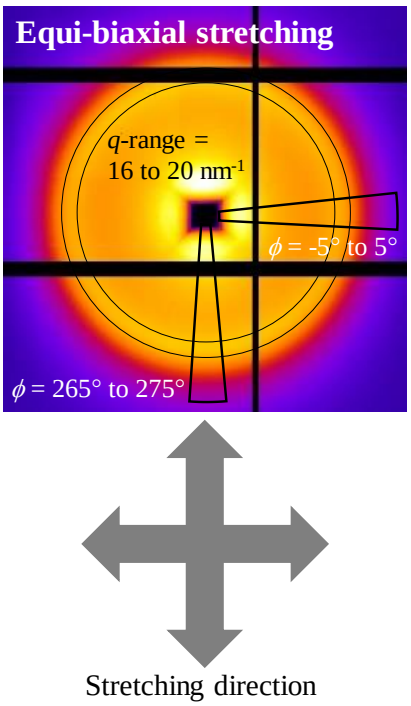

Figure 2A.5. *q*-range and azimuthal angle (ϕ) of WAXS results during equi-biaxial stretching, which were used to calculate the intensity ratio.

References

(1) Ariano, R. Rubber stretched by forces in two directions perpendicular to one another. *Rubber Chemistry and Technology* **1940**, *13*, 92-102.

(2) Bitoh, Y.; Akuzawa, N.; Urayama, K.; Takigawa, T. Strain energy function of swollen polybutadiene elastomers studied by general biaxial strain testing. *J. Polym. Sci. Part B: Polym. Phys.* **2010**, *48*, 721-728.

(3) Yohsuke, B.; Urayama, K.; Takigawa, T.; Ito, K. Biaxial strain testing of extremely soft polymer gels. *Soft Matter* **2011**, *7*, 2632-2638.

(4) Krishnan, A. S.; Van Zanten, J. H.; Seifert, S.; Lee, B.; Spontak, R. J. Selectively solvated triblock copolymer networks under biaxial strain. *Appl. Phys. Lett.* **2011**, *99*, 101908.

(5) Weidisch, R.; Stamm, M.; Michler, G.; Fischer, H.; Jérôme, R. Mechanical properties of weakly segregated block copolymers. 3. Influence of strain rate and temperature on tensile properties of poly (styrene-b-butyl methacrylate) diblock copolymers with different morphologies. *Macromolecules* **1999**, *32*, 742-750.

(6) Dair, B. J.; Honeker, C. C.; Alward, D. B.; Avgeropoulos, A.; Hadjichristidis, N.; Fetters, L. J.; Capel, M.; Thomas, E. L. Mechanical properties and deformation behavior of the double gyroid phase in unoriented thermoplastic elastomers. *Macromolecules* **1999**, *32*, 8145-8152.

(7) Stasiak, J.; Squires, A. M.; Castelletto, V.; Hamley, I. W.; Moggridge, G. D. Effect of stretching on the structure of cylinder- and sphere-forming styrene−isoprene−styrene block copolymers. *Macromolecules* **2009**, *42*, 5256-5265.

(8) Inoue, T.; Moritani, M.; Hashimoto, T.; Kawai, H. Deformation mechanism of elastomeric block copolymers having spherical domains of hard segments under uniaxial tensile stress. *Macromolecules* **1971**, *4*, 500-507.

(9) Brandt, M.; Ruland, W. SAXS studies on the deformation of macrolattices in block copolymers. *Acta Polym.* **1996**, *47*, 498-506.

(10) Huy, T. A.; Adhikari, R.; Michler, G. H. Deformation behavior of styrene-block-butadiene-block-styrene triblock copolymers having different morphologies. *Polymer* **2003**, *44*, 1247-1257.

(11) Stribeck, N.; Fakirov, S.; Apostolov, A. A.; Denchev, Z.; Gehrke, R. Deformation behavior of PET, PBT and PBT-based thermoplastic elastomers as revealed by SAXS from synchrotron. *Macromol. Chem. Phys.* **2003**, *204*, 1000-1013.

(12) Kojio, K.; Nakamura, S.; Furukawa, M. Effect of side methyl groups of polymer glycol on elongation-induced crystallization behavior of polyurethane elastomers. *Polymer* **2004**, *45*, 8147-8152.

(13) Kojio, K.; Nakamura, S.; Furukawa, M. Effect of side groups of polymer glycol on microphase-separated structure and mechanical properties of polyurethane elastomers. *J. Polym. Sci. Part B: Polym. Phys.* **2008**, *46*, 2054-2063.

(14) Kojio, K.; Matsuo, K.; Motokucho, S.; Yoshinaga, K.; Shimodaira, Y.; Kimura, K. Simultaneous small-angle X-ray scattering/wide-angle X-ray diffraction study of the microdomain structure of polyurethane elastomers during mechanical deformation. *Polym. J.* **2011**, *43*, 692.

(15) Matsumiya, Y.; Watanabe, H.; Takano, A.; Takahashi, Y. Uniaxial extensional behavior of (SIS)p-type multiblock copolymer systems: structural origin of high extensibility. *Macromolecules* **2013**, *46*, 2681-2695.

(16) McCready, E. M.; Burghardt, W. R. In situ SAXS studies of structural relaxation of an ordered block copolymer melt following cessation of uniaxial extensional flow. *Macromolecules* **2015**, *48*, 264-271.

(17) Tomita, S.; Lei, L.; Urushihara, Y.; Kuwamoto, S.; Matsushita, T.; Sakamoto, N.; Sasaki, S.; Sakurai, S. Strain-induced deformation of glassy spherical microdomains in elastomeric triblock copolymer films: simultaneous measurements of a stress–strain curve with 2d-SAXS patterns. *Macromolecules* **2017**, *50*, 677-686.

(18) Higaki, Y.; Suzuki, K.; Kiyoshima, Y.; Toda, T.; Nishiura, M.; Ohta, N.; Masunaga, H.; Hou, Z.; Takahara, A. Molecular aggregation states and physical properties of syndiotactic polystyrene/hydrogenated polyisoprene multiblock copolymers with crystalline hard domain. *Macromolecules* **2017**, *50*, 6184-6191.

(19) Hashimoto, T.; Fujimura, M.; Kawai, H. Domain-boundary structure of styrene-isoprene block copolymer films cast from solutions. 5. molecular-weight dependence of spherical microdomains. *Macromolecules* **1980**, *13*, 1660-1669.

(20) Hosemann, R.; Bagchi, S., Direct analysis of diffraction by matter. North-Holland Pub. Co.: 1962.

(21) Rahmawati, R.; Masuda, S.; Cheng, C.-H.; Nagano, C.; Nozaki, S.; Kamitani, K.; Kojio, K.; Takahara, A.; Shinohara, N.; Mita, K.; Uchida, K.; Yamasaki, S. Investigation of deformation behavior of thiourethane elastomers using in situ X-ray scattering, diffraction, and absorption methods. *Macromolecules* **2019**, *52*, 6825-6833.

(22) Caponetti, E.; Floriano, M.; Di Dio, E.; Triolo, R. On the shape of the radial distribution function of an assembly of monodisperse ellipsoidal scatterers. *J. Appl. Crystallogr.* **1993**, *26*, 612-615.

(23) Sheu, E. Y. Polydispersity analysis of scattering data from self-assembled systems. *Phys. Rev. A* **1992**, *45*, 2428-2438.

(24) Matsuoka, H.; Tanaka, H.; Iizuka, N.; Hashimoto, T.; Ise, N. Elastic scattering from cubic lattice systems with paracrystalline distortion. II. *Phys. Rev. B* **1990**, *41*, 3854.

(25) Matsuoka, H.; Tanaka, H.; Hashimoto, T.; Ise, N. Elastic scattering from cubic lattice systems with paracrystalline distortion. *Phys. Rev. B* **1987**, *36*, 1754.

(26) Uozumi, M.; Matsushita, T.; Sakamoto, N.; Yamazaki, T.; Imaizumi, K.; Li, L.; Urushihara, Y.; Kuwamoto, S.; Masunaga, H.; Sasaki, S. Changes in microphase-separated structures and properties of an elastomeric block copolymer film upon uniaxial stretching as analyzed by conducting simultaneous measurements of two-dimensional small-angle X-ray scattering with stress-strain tests. *Nihon Reoroji Gakkaishi* **2015**, *43*, 77-83.

(27) Tosaka, M.; Murakami, S.; Poompradub, S.; Kohjiya, S.; Ikeda, Y.; Toki, S.; Sics, I.; Hsiao, B. S. Orientation and crystallization of natural rubber network As revealed by WAXD using synchrotron radiation. *Macromolecules* **2004**, *37*, 3299-3309.

(28) Indukuri, K. K.; Lesser, A. J. Comparative deformational characteristics of poly(styrene-b-ethylene-co-butylene-b-styrene) thermoplastic elastomers and cross-linked natural rubber. *Polymer* **2005**, *46*, 7218-7229.

(29) Mamodia, M.; Indukuri, K.; Atkins, E. T.; De Jeu, W. H.; Lesser, A. J. Hierarchical description of deformation in block copolymer TPEs. *Journal of Materials Science* **2008**, *43*, 7035-7046.

Chapter 3

Microdomain Structure Change and Macroscopic Mechanical Response under Cyclic Uniaxial and Biaxial Stretching Modes

3.1 Introduction

The elastic property of elastomers is the ability that materials deformed by external force return to their original shape and size when the external force is removed. This elasticity originates from their network structures. During stretching, rubbery chains change their conformation from a gauche-rich to trans-rich state, leading to a decrease in entropy. This change in entropy produces a retractive force, which governs the elastic property of the elastomers [1]. Poly(styrene-*b*-ethylene-*co*-butylene-*b*-styrene) (SEBS) consists of a rubbery poly(ethylene-*co*-butylene) (PEB) midblock and glassy polystyrene (PS) end blocks [2-6]. Fractions of PS and PEB regulate the properties of SEBS. PS domains work as physical cross-linking points, whereas the PEB chains have high stretchability. There are two possible chain structures for midblocks: bridge and loop structures [7-8]. Bridge chains connect neighboring PS domains, whereas loop chains exist around the PS domain. As the fractions of bridge and loop chains are closely related to tensile properties, they must be considered [7-9].

When various types of rubber materials are subjected to cyclic deformation, hysteresis appears at a high strain during unloading. This phenomenon is well-known as the Mullins effect [10-14]. Several physical interpretations have been proposed to explain the Mullins effect, including bond rupture in the network structure, filler rupture, molecular slippage, and disentanglement. Rupture of the interaction between rubber and fillers is also a possible cause of the Mullins effect [15]. In the case of styrenic triblock copolymer elastomers, pulling out of the PS end blocks from their cross-linking points might be a cause of the Mullins effect. Most studies on the Mullins effect were discussed on the basis of cyclic uniaxial stretching. However, investigations only on the uniaxial stretching mode are insufficient to clarify the mechanical deformation behavior of elastomers [16-17]. The observation of the Mullins effect during various types of

deformation is essential to determine the softening behavior of elastomers [14, 18-21]. Urayama *et al*. investigated the Mullins effect for silica-filled-reinforced styrene butadiene rubbers under three types of extensions—uniaxial, planar and equi-biaxial extensions [21]. Energy dissipation and residual strain increased in the order of equi-biaxial, planar, and uniaxial extensions with increasing volume fraction of the fillers. They concluded that the rupture of the filler network and interaction between fillers and the rubber matrix are major factors governing the dissipation.

In Chapter 2, we have investigated the microdomain structure change in SEBS under two different deformation modes through small-angle X-ray scattering (SAXS) analysis, and observed that the contact of PS domains is one of the important factors governing the deformation behavior [6]. Synchrotron X-ray radiation SAXS measurements [22-32] can be utilized to identify the changes in the microdomain structure of elastomers during mechanical deformation in detail. However, the effect of cyclic deformation on the microdomain structures of SEBS has not been clarified yet. In this study, the effect of the stretching mode and cyclic stretching on the mechanical stretching behavior of SEBS, which is related to the Mullins effect, was investigated by *in situ* SAXS measurements.

3.2 Experiments

The procedure of the sample preparation was explained in section 2.2.1. Cyclic uniaxial and equi-biaxial tests were performed using custom-made uniaxial tensile tester (DIP Co.) and biaxial tester (JUNKEN MEDICAL Co., Ltd.), respectively. By using these testers, *in situ* SAXS measurements could be conducted. Film samples were stretched with loading–unloading cycles with increasing maximum stretching ratio (λ_m) for each cycle under uniaxial and equi-biaxial elongations at ~25 °C at 1 mm s^{-1}. For

cyclic uniaxial stretching, the sample was stretched to λ_m = 2.3, 3.6, 4.8, 6.1, and 7.4. For cyclic equi-biaxial stretching, the sample was stretched to λ_m = 2.3, 3.0, 3.6, and 4.2. *In situ* synchrotron SAXS measurements were performed at 25 °C at the beamlines at the SPring-8 facility in Japan (BL40XU and BL05XU). Figure 3.1 shows schematic illustration of experimental set-up of *in situ* SAXS measurements during cyclic uniaxial and equi-biaxial stretching. The wavelength and size of the X-rays were 0.100 nm and 150 × 150 μm^2, respectively. The camera length was ~2 m. The exposure time was 0.5–1.0 s. Two-dimensional (2D) SAXS patterns were obtained using a PILATUS 100k detector (DECTRIS, Ltd.). One-dimensional (1D) profiles along directions parallel and perpendicular to the stretching direction were obtained using the FIT2D software (ver. 16.041, Andy Hammersley/ESRF, Grenoble, France).

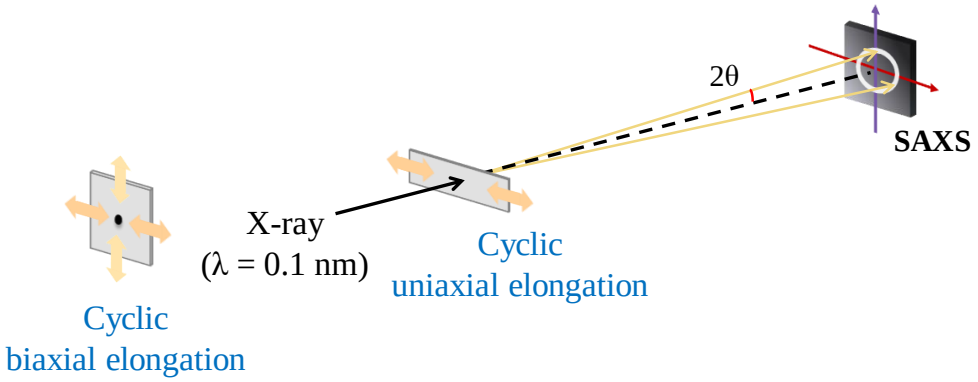

Figure 3.1. Schematic illustration of experimental set-up of *in situ* SAXS measurements during cyclic uniaxial and equi-biaxial stretching.

3.3 Results and discussion

3.3.1 Strain energy density function analysis

Several models of strain energy density function (W) were considered to investigate the factors governing the mechanical properties of samples [17, 33-37]. In this study, the W

values of the four models were investigated on the basis of the stress and stretching ratio (λ) relationship of equi-biaxial stretching and planar extension of SEBS. The molecular weights, polydispersity index, and glass transition temperature (T_g) of SEBS are summarized in Table 1. The films were stretched along the X-axis (λ_x) while maintaining the initial dimension along the Y-axis ($\lambda_y = 1$) under the planar extension mode. The classical neo-Hookean model was initially explored as it is the simplest model among other existing constitutive models. This model describes ideal rubber networks with infinite extensibility without structural defects. There is no change in volume, and $\lambda_x\lambda_y\lambda_z = 1$ is satisfied. As SEBS exhibited strain hardening in the high-deformation region, which is a characteristic of non-Gaussian statistics, Gent, extended Gent [34], and Ogden models [17, 36] were applied to investigate the relationship of stress and λ of SEBS, as they have been used to describe the non-linear elasticity of various elastomeric materials. *W* of neo-Hookean model is given by

$$W = \frac{G}{2}\left({\lambda_x}^2 + {\lambda_y}^2 + {\lambda_z}^2 - 3\right) = \frac{G}{2}(I_1 - 3) \tag{3.1}$$

where *G* is shear modulus, λ_i ($i = x, y, z$) is principal extension ratio and I_1 is the first invariant of the Green's deformation tensor, respectively. The stress–λ relationships of neo-Hookean model are shown in following equations:

$$\sigma_{EB} = G\left(\lambda_x - {\lambda_x}^{-5}\right) \tag{3.2}$$

$$\sigma_{PE-X} = G\left(\lambda_x - {\lambda_x}^{-3}\right) \tag{3.3}$$

$$\sigma_{PE-Y} = G\left(1 - {\lambda_x}^{-2}\right) \tag{3.4}$$

σ_{EB}, σ_{PE-X} and σ_{PE-Y} are defined as stress of biaxial stretching, planar extension in X- and Y-axes, respectively. Since SEBS showed strain hardening at high deformation region which is a characteristic of non-Gaussian statistics, Gent, extended Gent [34] and

Ogden models [17, 36] were applied to investigate the relationship of stress and λ of SEBS as they have been used to describe the non-linear elasticity of various elastomeric materials. Strain energy density function of the Gent model is expressed as [33-34]

$$W = -\frac{G}{2}(I_m - 3)ln\left(1 - \frac{I_1 - 3}{I_m - 3}\right) \quad (3.5)$$

The relationship of stress–λ in the Gent model is given as

$$\sigma_{EB} = \frac{G(\lambda_x - {\lambda_x}^{-5})}{1-(2{\lambda_x}^2 - {\lambda_x}^{-4} - 3)/(I_m - 3)} \quad (3.6)$$

$$\sigma_{PE-X} = \frac{G(\lambda_x - {\lambda_x}^{-3})}{1-({\lambda_x}^2 - {\lambda_x}^{-2} - 2)/(I_m - 3)} \quad (3.7)$$

$$\sigma_{PE-Y} = \frac{G(1 - {\lambda_x}^{-2})}{1-({\lambda_x}^2 - {\lambda_x}^{-2} - 2)/(I_m - 3)} \quad (3.8)$$

I_m is the maximum value of I_1 in biaxial stretching and planar extension modes where the stress becomes infinite. The extended Gent model was proposed as a sum of Gent model and a linear term of the second invariant of Green's deformation tensor (I_2), where $I_2 = {\lambda_x}^2{\lambda_y}^2 + {\lambda_y}^2{\lambda_z}^2 + {\lambda_z}^2{\lambda_x}^2$. Strain energy density function in the addition of I_2 is the function that can explain the strain-coupling effect, given in the following equation:

$$W = -\frac{C_1}{2}(I_m - 3)ln\left(1 - \frac{I_1 - 3}{I_m - 3}\right) + \frac{C_2}{2}(I_2 - 3) \quad (3.9)$$

The stress–λ relationship of each deformation mode in extended Gent model is expressed as

$$\sigma_{EB} = \frac{C_1(\lambda_x - {\lambda_x}^{-5})}{1-(2{\lambda_x}^2 - {\lambda_x}^{-4} - 3)/(I_m - 3)} + C_2({\lambda_x}^3 - {\lambda_x}^{-3}) \quad (3.10)$$

$$\sigma_{PE-X} = \frac{C_1(\lambda_x - {\lambda_x}^{-3})}{1-({\lambda_x}^2 - {\lambda_x}^{-2} - 2)/(I_m - 3)} + C_2(\lambda_x - {\lambda_x}^{-3}) \quad (3.11)$$

$$\sigma_{PE-Y} = \frac{C_1(1 - {\lambda_x}^{-2})}{1-({\lambda_x}^2 - {\lambda_x}^{-2} - 2)/(I_m - 3)} + C_2({\lambda_x}^2 - 1) \quad (3.12)$$

C_1 and C_2 are the fitting parameter, which were independently. The C_1 and C_2 are related to G, as $G = C_1+C_2$. C_1 is almost the same value of G and C_2 is related to the stress coupling of different axes. W of the Ogden model is expressed as

$$W = \sum_n \frac{\mu_n}{\alpha_n}\left({\lambda_x}^{\alpha_n} + {\lambda_y}^{\alpha_n} + {\lambda_z}^{\alpha_n} - 3\right) \quad (3.13)$$

Additional terms μ and α were introduced to achieve a good fit to the experimental data. The stress–λ relationships of the Ogden model are shown in the following equations:

$$\sigma_{EB} = \frac{1}{\lambda_x}\sum_n \mu_n\left({\lambda_x}^{\alpha_n} - {\lambda_x}^{-2\alpha_n}\right) \quad (3.14)$$

$$\sigma_{PE-X} = \frac{1}{\lambda_x}\sum_n \mu_n({\lambda_x}^{\alpha_n} - {\lambda_x}^{-\alpha_n}) \quad (3.15)$$

$$\sigma_{PE-Y} = \sum_n \mu_n(1 - {\lambda_x}^{-\alpha_n}) \quad (3.16)$$

σ_{EB}, σ_{PE-X} and σ_{PE-Y} are defined as stress of equi-biaxial stretching, planar extension in X- and Y-axes, respectively.

Figure 3.2 illustrates (a) the relationships between λ and the stress of SEBS during equi-biaxial stretching and planar extension and (b) the data in the small λ region, respectively. The initial moduli of equi-biaxial stretching and planar extension in the X- and Y-axes were consistent with the infinitesimal linear elasticity theory, as these moduli were approximately 6G, 4G, and 2G, respectively [38]. Plots of the model analysis are shown in Figure 3.3. As shown in Figure 3.3 (a), the prediction of the neo-Hookean model did not fit the experimental data. This is because the tensile properties of SEBS were not consistent with the assumptions of this model. Considering the finite extensibility effect, Gent, extended Gent, and Ogden models were introduced to determine the tensile properties of SEBS. From Figure 3.3 (b), the Gent model did not fit well with the experimental data of SEBS, indicating that additional factors should be considered. The value of stress ratio (σ_y/σ_x) of the planar extension test with various λ_x

was calculated to investigate the coupling between the X- and Y-axes, as shown in Figure 3.3 (e). It was found that σ_y/σ_x lies above the predictions of the neo-Hookean and Gent models (dashed line), suggesting that the cross-effect of strains in different directions affects the deformation of SEBS. The cross-effect is represented by the second invariant of the deformation tensor (I_2) and observed by specific entanglement, excluded volume effect, and other aspects. Therefore, an extended Gent model considering the cross-effect of strain represented by I_2 was applied. However, as shown in Figure 3.3 (c), the extended Gent model was not in good agreement with the experimental data of SEBS. The advantage of Gent and extended Gent models is that the parameters from these models can be interpreted as the molecular properties of elastomers; however, they are unable to predict the properties in the entire range of strain of SEBS. Therefore, the Ogden model was employed in this study. The set of parameters μ and α was determined as a constant value for each sample, which was independent of the deformation mode. The number of terms μ and α were included by summation to yield a good fitting result to the experimental data. As shown in Figure 3.3 (d), the experimental data of SEBS during equi-biaxial stretching and planar extension tests were satisfactorily described by the Ogden model using two terms (n=2) of the parameter set of μ and α. The constant values of $\mu_1 = 1.2$ and $\alpha_1 = 0.25$ along with $\mu_2 = 0.29$ and $\alpha_2 = 2.22$ showed the best fit with the experimental data of SEBS.

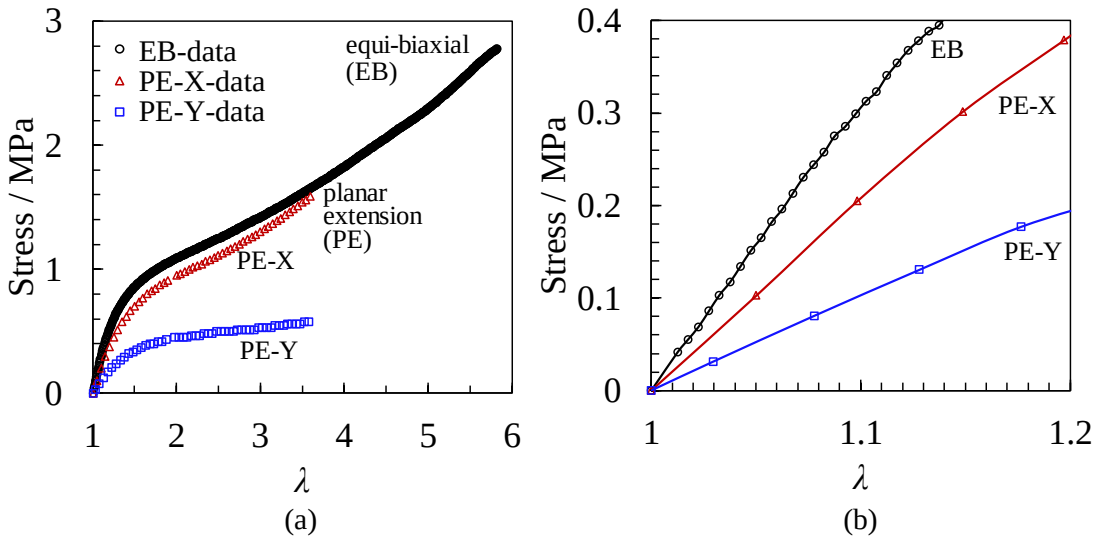

Figure 3.2. (a) Relationships between λ and stress of SEBS during equi-biaxial stretching and planar extension (experimental data). (b) Data of (a) at a small deformation region.

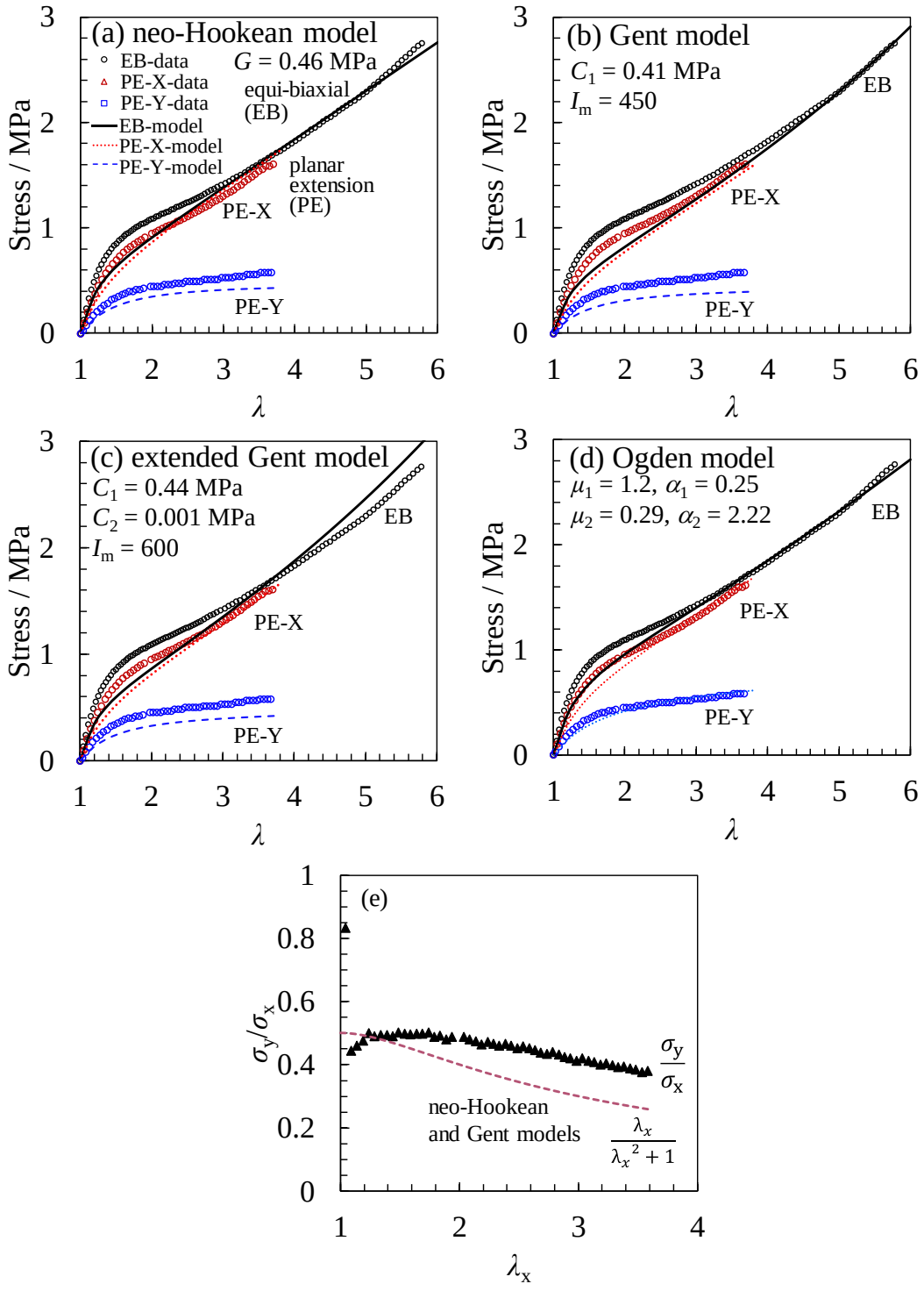

Figure 3.3. Relationships between real λ and stress of SEBS during equi-biaxial stretching and planar extension. Line curves correspond to the prediction of (a) neo-Hookean, (b) Gent, (c) extended Gent and (d) Ogden models. (e) Stress ratio (σ_y/σ_x) as a function of λ_x in planar extension of SEBS. The dashed line is the prediction of the neo-Hookean and Gent models.

3.3.2 Stress–λ relationship of SEBS during cyclic stretching

To investigate the mechanical stretching behavior of SEBS, films were stretched with loading–unloading cycles of various λ_ms under uniaxial and equi-biaxial elongations at 25 °C. Figure 3.4 (a) and (b) show the stress–λ relationship of cyclic uniaxial and equi-biaxial stretching at 1 mm s^{-1} and 25 °C, respectively. The stress during unloading processes exhibited smaller magnitudes than during the loading processes for cyclic uniaxial stretching, as shown in Figure 3.4 (a). This decrement became larger with increasing λ_m. The permanent set also increased with increasing λ_m. In contrast, the stress during the loading and unloading processes exhibited similar values for cyclic equi-biaxial stretching and smaller permanent sets, as shown in Figure 3.4 (b). In other words, the hysteresis for the cyclic equi-biaxial stretching mode was smaller than that for the cyclic uniaxial stretching mode.

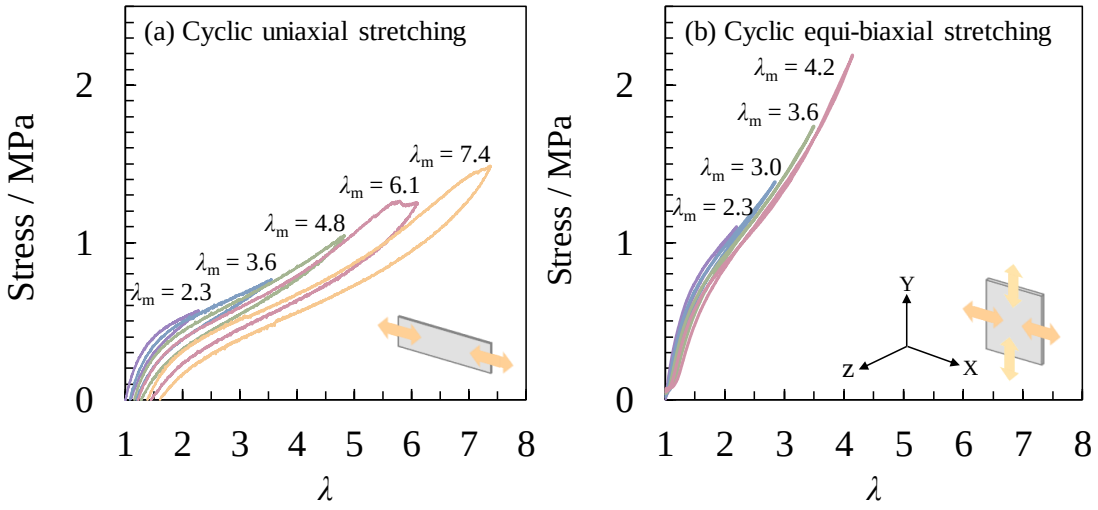

Figure 3.4. Stress–λ relationship of SEBS under (a) cyclic uniaxial stretching and (b) cyclic equi-biaxial stretching at 1 mm s^{-1} and 25 °C.

Quantitative analysis was performed to discuss the hysteresis of the two deformation modes based on the calculation of dissipation energy (*D*). Figure 3.5 shows the relationship between the dissipation factor (Δ) and λ_m of each cycle of cyclic uniaxial and equi-biaxial elongations. Δ, calculated from the ratio of *D* to stored elastic energy in the virgin loading process (W_0), can be used to compare *D* of different deformation modes and λ with respect to W_0 [21]. *D* is the energy consumption of the rubber chains during cyclic deformation, thus a high *D* indicates high hysteresis. The equations are as follows:

$$\Delta = \frac{D}{W_0} \tag{3.17}$$

$$D = W_{load} - W_{unload} \tag{3.18}$$

where W_{load} and W_{unload} are the stored elastic energy in the loading process and released elastic energy in the unloading process, respectively. For the cyclic uniaxial stretching, Δ increased with increasing λ_m of each cycle, which was not observed for the cyclic equi-biaxial stretching. This difference in the energy dissipation for the two modes was suggested to be mainly from the network of PEB chains, which impart stretchability to SEBS. Energy loss in SEBS during the cyclic test could be a result of irreversible structural changes during deformation, such as pulling out and slipping of PEB chains from the PS domains. A detailed discussion will be provided in a later section.

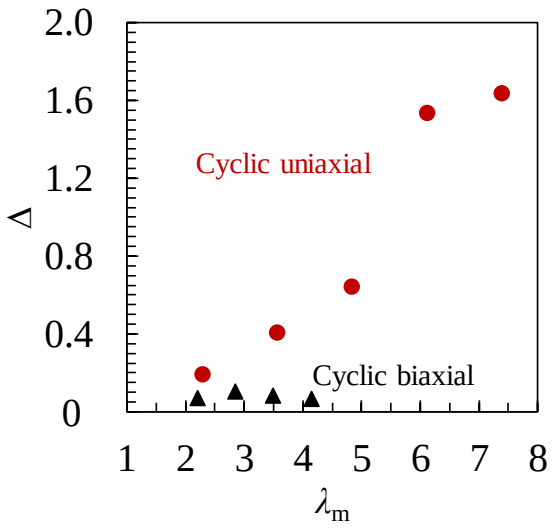

Figure 3.5. Relationship between Δ and λ_m of each cycle during cyclic uniaxial and equi-biaxial stretching at 1 mm s^{-1}.

3.3.3 Microdomain structure change of SEBS during cyclic stretching

In situ SAXS measurements were carried out to investigate the arrangement of PS domains. Figure 2.4 in Chapter 2 shows the SAXS patterns and profiles of SEBS before and after annealing. The 2D SAXS pattern of the annealed sample exhibited three sharp rings. This indicates that the crystal grain size is smaller than the size of the X-ray beam, and the grains are randomly oriented. The peak positions of these three peaks were at q = 0.26, 0.36, and 0.45 nm^{-1}, and correspond to the (110), (200), and (211) planes of the body-centered cubic (bcc) lattice, respectively [39]. Moreover, periodic intensity fluctuations were observed in the profiles, which correspond to the form factor scattered from the spherical PS domains.

As stated above, SAXS data can provide information about the changes in the microdomain structure, including spacing, ordering, and shape of PS domains during mechanical deformation. Thus, it is useful to discuss the mechanical deformation behavior of SEBS by comparing microscopic and macroscopic experimental data.

Figures 3.6 and 3.7 show the SAXS patterns and profiles of SEBS during cyclic uniaxial and equi-biaxial stretching, respectively. Discussion of the cyclic uniaxial stretching mode will refer only to the arrangement of PS domains along the stretching direction. Three diffraction peaks shifted to the lower q region during the loading process and continuously shifted back during the unloading process. These shifts imply a change in the plane spacing (d) during stretching. Thus, the plane spacing of the PS domains increased with increasing λ during the loading process and decreased with decreasing λ during the unloading process. In the case of cyclic equi-biaxial stretching mode, three diffraction peaks shifted to the lower q region during the loading process and shifted back during the unloading process. However, it was found that the position of the diffraction peaks after the unloading process of each cycle slightly shifted to the lower q region. This shift of the diffraction peaks from an initial position implies that the plane spacing of PS domains did not completely return to its original position; however, it slightly increased after the unloading process. An increase in the plane spacing implies that residual λ slightly occurred in the structure of SEBS during cyclic equi-biaxial stretching.

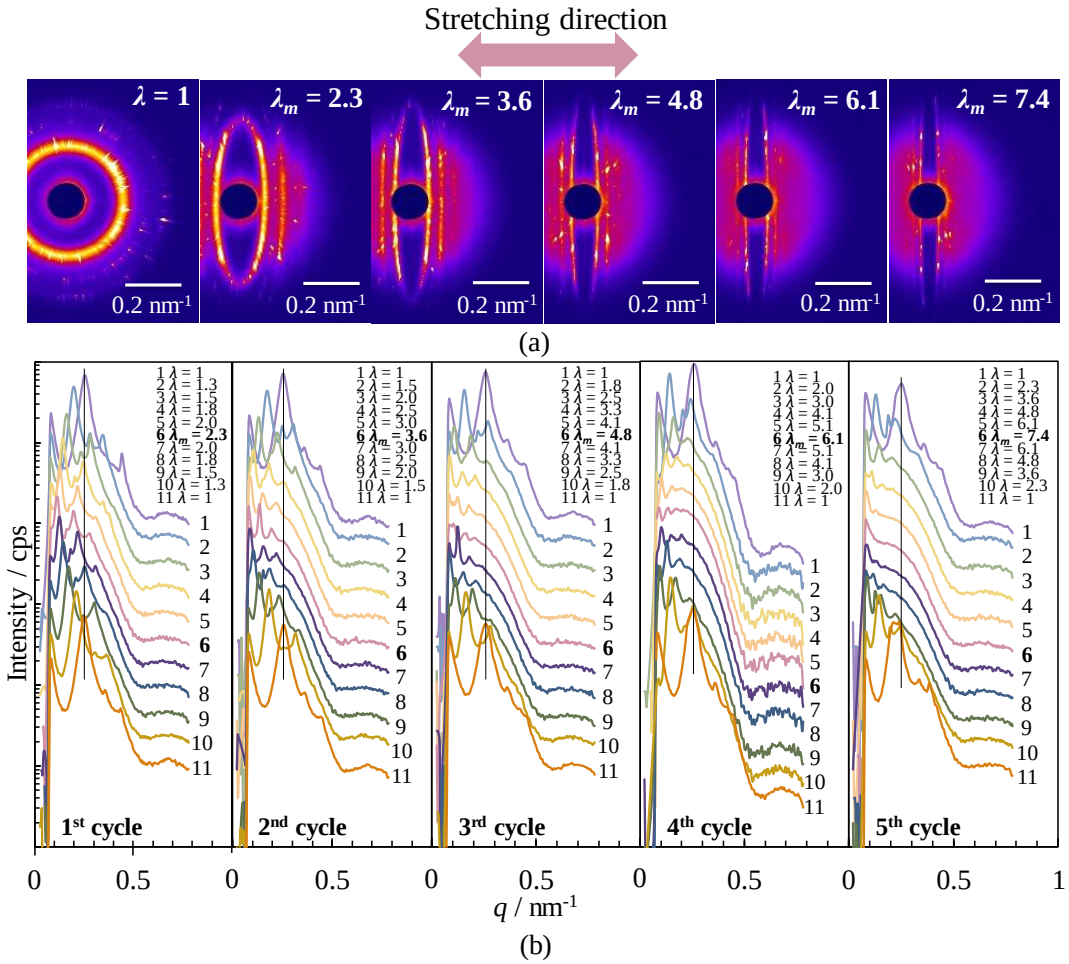

Figure 3.6. (a) SAXS patterns of SEBS during cyclic uniaxial stretching at 1 mm s^{-1} and 25 °C at various λs; (b) profiles obtained from (a) in the stretching direction.

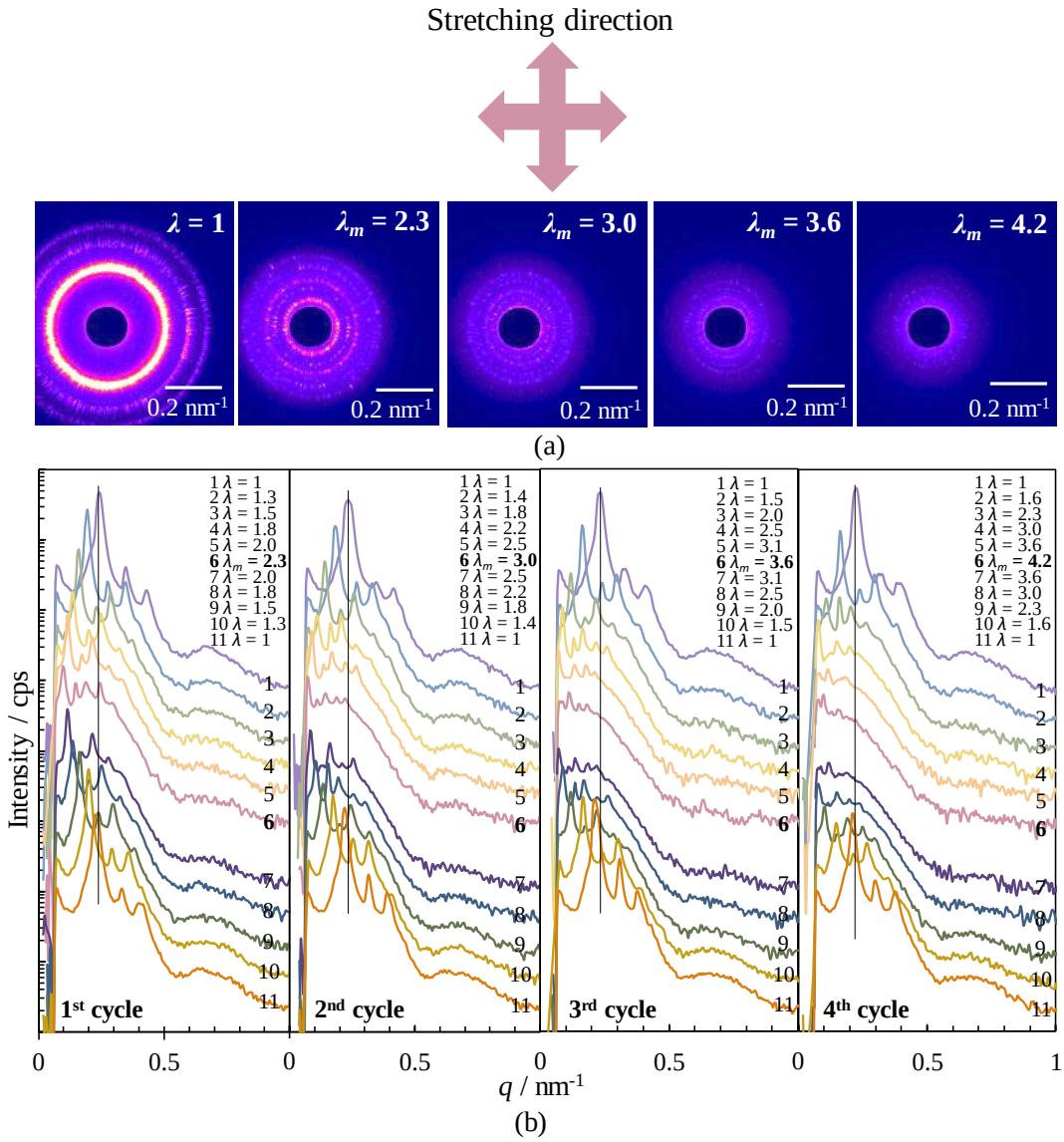

Figure 3.7. (a) SAXS patterns of SEBS during cyclic equi-biaxial stretching at 1 mm s^{-1} and 25 °C at various λs; (b) profiles obtained from (a) in the X-axis.

Figure 3.8 (a) shows the relationship between λ and λ of the (110) plane spacing obtained from SAXS ($\lambda_{SAXS(110)}$) during cyclic uniaxial stretching. The diagonal line in Figure 3.8 (a) corresponds to the affine deformation. During the first loading of cyclic uniaxial stretching (λ_m = 2.3), SEBS showed affine deformation. Deviation from the affine deformation was observed with increasing λ_m. This indicates that the ordering of the arrangement of PS domains disrupted. Irreversible structural changes, such as pulling

out of PS end blocks, rupture of PEB chains, and rupture of PS domains, might have occurred during cyclic stretching. This irreversibility was correlated with the deviation of the arrangement of PS domains from the affine deformation. The degree of deviation increased with increasing λ_m. The λ_{SAXS} of the unloading process showed a slightly larger deviation than the loading process of each cycle. This result was correlated with the hysteresis observed from the curves of the stress–λ relationship.

Figure 3.8 (b) shows λ of plane spacing obtained from SAXS (λ_{SAXS}) with various orientation angles of the crystal plane (ω) during cyclic uniaxial stretching. The deviation was observed in various orientations of the crystal plane in SEBS, as shown in Figure 3.8 (b). The λ_{SAXS} measured at various ω at λ = 1.51 and 2.28 of the first loading showed good agreement with the theoretical curve of the affine deformation (line curves), which was calculated from equation (3.19) [40].

$$\lambda_{\text{theory SAXS}} = [{\alpha_x}^2 cos^2\omega + (1/\alpha_x) sin^2\omega]^{1/2} \quad (3.19)$$

where α_x is the macroscopic strain and ω is the orientation angle of the crystal plane. An additional explanation is included in Figure 3.9. In contrast, the λ_{SAXS} measured during unloading and reloading processes clearly deviated from the theoretical affine deformation curve for various orientations of the crystal plane. At λ = 4.84 of the third cycle, the deviation from the affine deformation was clearly observed.

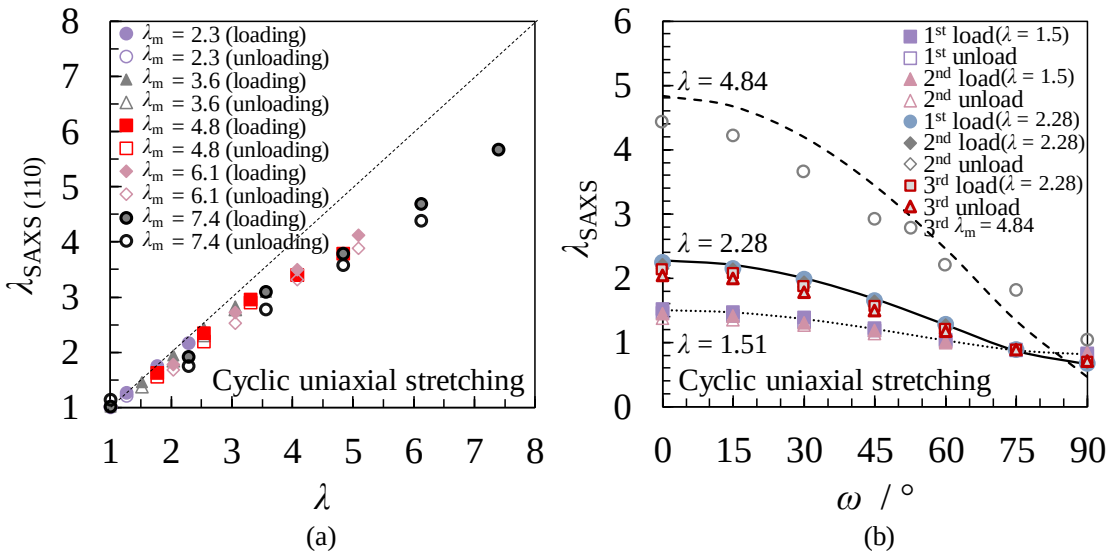

Figure 3.8. Relationship between (a) λ of SEBS and $\lambda_{SAXS(110)}$ obtained during cyclic uniaxial stretching at 1 mm s^{-1}, (b) λ_{SAXS} with various ω values during cyclic uniaxial stretching at 1 mm s^{-1}. Line plots are the theoretical curves of the affine deformation.

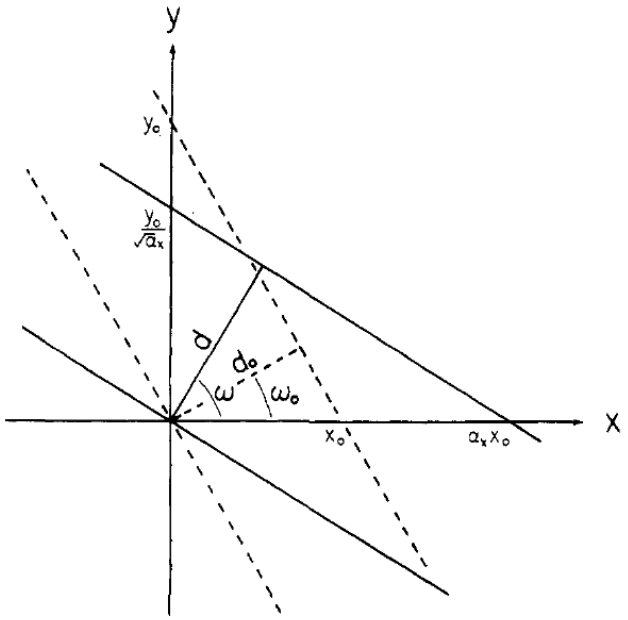

Figure 3.9. 2D analysis for the change in the $\lambda_{theorySAXS}$ between two consecutive diffracting planes in grains undergoing an affine deformation with respect to the strain ellipsoid model [40].

Figure 3.10 shows the relationship between λ and λ_{SAXS} at λ_ms of 2.3, 3.0, 3.6, and 4.2 during cyclic equi-biaxial stretching. In this case, SEBS also showed affine deformations in the small λ region. Then, the deviation slightly occurred with increasing λ_m. However, the deviation during cyclic equi-biaxial stretching was smaller than that during cyclic uniaxial stretching. Furthermore, in the larger strain region, the crystal plane dependence on the deviation from affine deformation was observed during cyclic equi-biaxial deformation. Figure 3.11 shows a schematic illustration of the arrangement of PS domains in (110), (200), (211), (220), and (310) crystal planes of the bcc lattice. Crystal planes with small periods, such as (220) and (310), tended to show large deviations. Several PEB bridge chains seems to exist at the 1st and 2nd nearest positions between PS domains ($(\sqrt{3}/2)a$ and a), where a is the lattice length of the bcc lattice. For the (110), (200), and (211) planes, the direction of bridges is almost perpendicular to each plane, whereas that for (310) is almost parallel. Furthermore, the number of PEB chains between each (310) plane is smaller compared to that between other planes, and there are no PEB chains between PS domains placed in the (310) planes. Thus, the elastic property of the (310) planes might be lower than those of the (110), (200), and (211) planes, resulting in larger deviation of (310) from affine deformation.

The smaller hysteresis and deviation from the affine deformation of the cyclic equi-biaxial stretching mode can be discussed on the basis of the relationship between the types of PEB bridge chains and the cross-effect of strain. There are three types of PEB bridge chains between the PS domains in SEBS. These are defined as the 1st, 2nd, and 3rd nearest PS domains, and their distances are $(\sqrt{3}/2)a$, a, and $\sqrt{2}a$, respectively, where a is the lattice length of the bcc lattice. These different distances between PS domains may have caused the deviation of σ_y/σ_x from the prediction of the neo-Hookean and Gent models, as shown in Figure 3.3 (e). Furthermore, a specific entanglement effect

may exist, which could be attributed to the entangled loops. Figure 3.12 shows a schematic illustration of the occurrence of nominal cross-linking points during equi-biaxial stretching. For SEBS, the entangled loop effect seemed to be more evident during equi-biaxial stretching than uniaxial stretching. This entangled loop effect might be induced by the topological effect during equi-biaxial stretching. Entangled loop of PEB chains might serve as additional cross-linking points to the physical one, PS domains, resulting in smaller hysteresis during equi-biaxial stretching.

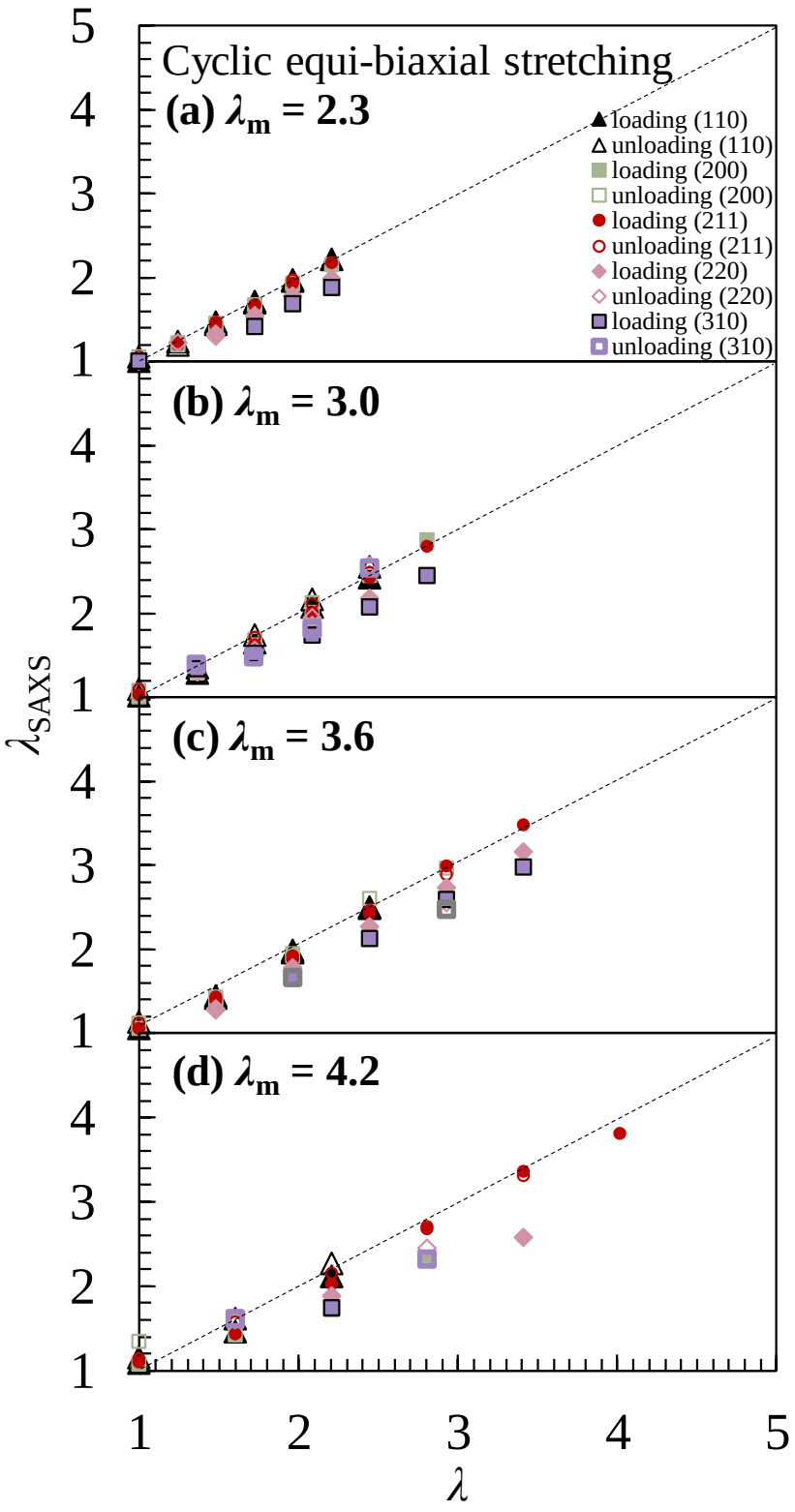

Figure 3.10. Relationship between λ and λ_{SAXS} with various λ_ms of (a) 2.3, (b) 3.0, (c) 3.6, and (d) 4.2 of each cycle during cyclic equi-biaxial stretching at 1 mm s^{-1}.

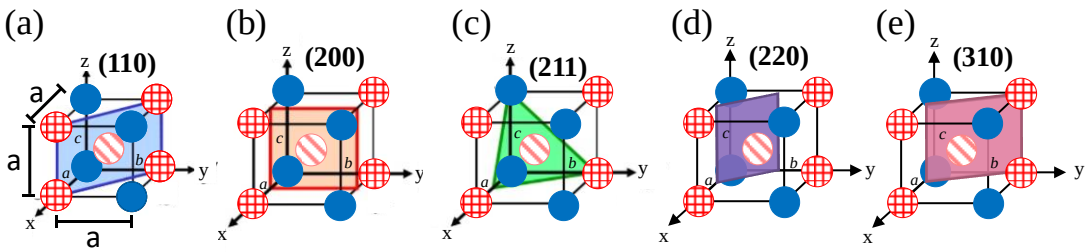

Figure 3.11. Schematic illustration of the arrangement of PS domains in (a) (110), (b) (200), (c) (211), (d) (220) and (e) (310) crystal planes of the bcc lattice.

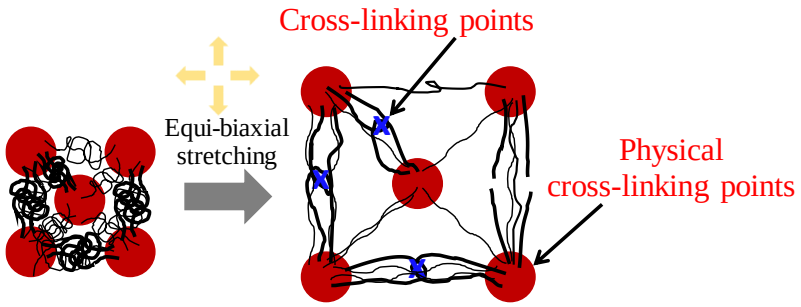

Figure 3.12. Schematic illustration of the occurrence of nominal cross-linking points during equi-biaxial stretching.

3.4 Conclusions

The mechanical stretching behavior of SEBS was investigated under three different stretching modes and by *in situ* SAXS measurements. The cross-effect of strain represented by I_2 was observed, and the Ogden model could only express the experimental stress–λ curve. Hysteresis, so-called the Mullins effect, and deviation from the affine deformation were observed in the cyclic stretching test. Cyclic equi-biaxial stretching exhibited smaller hysteresis and deviation from the affine deformation than cyclic uniaxial stretching. The cross-effect of strains in different directions may be attributed to the (1) existence of three different lengths of PEB bridge chains between PS domains, (2) pulling out of PS end blocks from PS domains, and (3) presence of the

entangled loop. The entangled loop effect might be the main factor for small hysteresis and deviation from affine deformation during equi-biaxial stretching.

References

(1) Treloar, L. The physics of rubber elasticity. Oxford University Press, USA: 1975.

(2) Sohn, K. E.; Kojio, K.; Berry, B. C.; Karim, A.; Coffin, R. C.; Bazan, G. C.; Kramer, E. J.; Sprung, M.; Wang, J. Surface effects on the thin film morphology of block copolymers with bulk order−order transitions. *Macromolecules* **2010**, *43*, 3406-3414.

(3) Tomita, S.; Lei, L.; Urushihara, Y.; Kuwamoto, S.; Matsushita, T.; Sakamoto, N.; Sasaki, S.; Sakurai, S. Strain-induced deformation of glassy spherical microdomains in elastomeric triblock copolymer films: simultaneous measurements of a stress–strain curve with 2d-SAXS patterns. *Macromolecules* **2017**, *50*, 677-686.

(4) Morita, H.; Miyamoto, A.; Kotani, M. Recoverably and destructively deformed domain structures in elongation process of thermoplastic elastomer analyzed by graph theory. *Polymer* **2020**, *188*, 122098.

(5) Liu, H.; Liang, X.; Nakajima, K. Direct visualization of a strain-induced dynamic stress network in a SEBS thermoplastic elastomer with in situ AFM nanomechanics. *Jpn. J. Appl. Phys* **2020**.

(6) Dechnarong, N.; Kamitani, K.; Cheng, C.-H.; Masuda, S.; Nozaki, S.; Nagano, C.; Amamoto, Y.; Kojio, K.; Takahara, A. In situ synchrotron radiation X-ray scattering investigation of a microphase-separated structure of thermoplastic elastomers under uniaxial and equi-biaxial deformation modes. *Macromolecules* **2020**, *53*, 8901-8909.

(7) Watanabe, H.; Sato, T.; Osaki, K. Concentration dependence of loop fraction in styrene−isoprene−styrene triblock copolymer solutions and corresponding changes in equilibrium elasticity. *Macromolecules* **2000**, *33*, 2545-2550.

(8) Watanabe, H.; Matsumiya, Y.; Sawada, T.; Iwamoto, T. Rheological and dielectric behavior of dipole-inverted (SIS)p-type multiblock copolymers: estimates of bridge/loop fractions for respective I blocks and effect of loops on high extensibility of bridges. *Macromolecules* **2007**, *40*, 6885-6897.

(9) Takahashi, Y.; Song, Y.; Nemoto, N.; Takano, A.; Akazawa, Y.; Matsushita, Y. Effect of loop/bridge conformation ratio on elastic properties of the sphere-forming ABA triblock copolymers under uniaxial elongation. *Macromolecules* **2005**, *38*, 9724-9729.

(10) Mullins, L. Effect of stretching on the properties of rubber. *Rubber Chem. Technol.* **1948**, *21*, 281-300.

(11) Mullins, L.; Tobin, N. R. Theoretical model for the elastic behavior of filler-reinforced vulcanized rubbers. *Rubber Chem. Technol.* **1957**, *30*, 555-571.

(12) Mullins, L. Softening of rubber by deformation. *Rubber Chem. Technol.* **1969**, *42*, 339-362.

(13) Kakavas, P. A. Mechanical properties of bonded elastomer discs subjected to triaxial stress. *J. Appl. Polym. Sci.* **1996**, *59*, 251-261.

(14) Cho, H.; Mayer, S.; Pöselt, E.; Susoff, M.; Veld, P.; Rutledge, G. C.; Boyce, M. C. Deformation mechanisms of thermoplastic elastomers: Stress-strain behavior and constitutive modeling. *Polymer* **2017**, *128*, 87-99.

(15) Bueche, F. Molecular basis for the Mullins effect. *J. Appl. Polym. Sci.* **1960**, *4*, 107-114.

(16) Obata, Y.; Kawabata, S.; Kawai, H. Mechanical properties of natural rubber vulcanizates in finite deformation. *J Polym Sci A-2 Polym Phys* **1970**, *8*, 903-919.

(17) Bitoh, Y.; Akuzawa, N.; Urayama, K.; Takigawa, T. Strain energy function of swollen polybutadiene elastomers studied by general biaxial strain testing. *J. Polym. Sci. Part B: Polym. Phys.* **2010**, *48*, 721-728.

(18) Ogden, R. W.; Roxburgh, D. G. A pseudo elastic model for the Mullins effect in filled rubber. *Proc. R. Soc. A* **1999**, *455*, 2861-2877.

(19) Webber, R. E.; Creton, C.; Brown, H. R.; Gong, J. P. Large strain hysteresis and mullins effect of tough double-network hydrogels. *Macromolecules* **2007**, *40*, 2919-2927.

(20) Dorfmann, A.; Pancheri, F. Q. A constitutive model for the Mullins effect with changes in material symmetry. *Int J Non Linear Mech.* **2012**, *47*, 874-887.

(21) Mai, T.-T.; Morishita, Y.; Urayama, K. Novel features of the Mullins effect in filled elastomers revealed by stretching measurements in various geometries. *Soft Matter* **2017**, *13*, 1966-1977.

(22) Kojio, K.; Matsuo, K.; Motokucho, S.; Yoshinaga, K.; Shimodaira, Y.; Kimura, K. Simultaneous small-angle X-ray scattering/wide-angle X-ray diffraction study of the microdomain structure of polyurethane elastomers during mechanical deformation. *Polym. J.* **2011**, *43*, 692.

(23) McCready, E. M.; Burghardt, W. R. In situ SAXS studies of structural relaxation of an ordered block copolymer melt following cessation of uniaxial extensional flow. *Macromolecules* **2015**, *48*, 264-271.

(24) Nozaki, S.; Masuda, S.; Kamitani, K.; Kojio, K.; Takahara, A.; Kuwamura, G.; Hasegawa, D.; Moorthi, K.; Mita, K.; Yamasaki, S. Superior properties of polyurethane elastomers synthesized with aliphatic diisocyanate bearing a symmetric structure. *Macromolecules* **2017**, *50*, 1008-1015.

(25) Rahmawati, R.; Nozaki, S.; Kojio, K.; Takahara, A.; Shinohara, N.; Yamasaki, S. Microphase-separated structure and mechanical properties of cycloaliphatic diisocyanate-based thiourethane elastomers. *Polym. J.* **2018**, *51*, 265-273.

(26) Doi, T.; Takagi, H.; Shimizu, N.; Igarashi, N.; Sakurai, S. Effects of drying temperature in solution coating process on the structural changes upon uniaxial stretching of sphere-forming block copolymer films. *Polym. J.* **2019**, *52*, 421-433.

(27) Rahmawati, R.; Masuda, S.; Cheng, C.-H.; Nagano, C.; Nozaki, S.; Kamitani, K.; Kojio, K.; Takahara, A.; Shinohara, N.; Mita, K.; Uchida, K.; Yamasaki, S. Investigation of deformation behavior of thiourethane elastomers using in situ X-ray scattering, diffraction, and absorption methods. *Macromolecules* **2019**, *52*, 6825-6833.

(28) Shinohara, Y.; Kishimoto, H.; Masui, T.; Hattori, S.; Yamaguchi, N.; Amemiya, Y. Microscopic structural response of nanoparticles in styrene–butadiene rubber under cyclic uniaxial elongation. *Polym. J.* **2019**, *51*, 161-171.

(29) Kitamura, Y.; Okada, K.; Masunaga, H.; Hikosaka, M. Role of strain rate in the strain-induced crystallization (SIC) of natural and synthetic isoprene rubber. *Polym. J.* **2019**, *51*, 221-226.

(30) Shen, J.; Sugimoto, I.; Matsumoto, T.; Horike, S.; Koshiba, Y.; Ishida, K.; Mori, A.; Nishino, T. Fabrication and characterization of elastomeric semiconductive thiophene polymers by peroxide crosslinking. *Polym. J.* **2019**, *51*, 257-263.

(31) Ishige, R. Precise structural analysis of polymer materials using synchrotron X-ray scattering and spectroscopic methods. *Polym. J.* **2020**, *52*, 1013-1026.

(32) Tamura, E.; Kume, T.; Okamoto, S.; Inoue, T. A rheo-optical study on the linear viscoelasticity and molecular dynamics of block copolymer solutions forming hexagonal close-packed cylindrical domains. *Polym. J.* **2020**, *52*, 1085-1091.

(33) Gent, A. N. A new constitutive relation for rubber. *Rubber Chem. Technol.* **1996**, *69*, 59-61.

(34) Katashima, T.; Urayama, K.; Chung, U.-i.; Sakai, T. Strain energy density function of a near-ideal polymer network estimated by biaxial deformation of Tetra-PEG gel. *Soft Matter* **2012**, *8*, 8217.

(35) Akagi, Y.; Katashima, T.; Sakurai, H.; Chung, U.-i.; Sakai, T. Ultimate elongation of polymer gels with controlled network structure. *RSC Adv.* **2013**, *3*, 13251-13258.

(36) Ogden, R. W.; Hill, R. Large deformation isotropic elasticity - on the correlation of theory and experiment for incompressible rubberlike solids. *Proc. R. Soc. A* **1972**, *326*, 565-584.

(37) Yohsuke, B.; Urayama, K.; Takigawa, T.; Ito, K. Biaxial strain testing of extremely soft polymer gels. *Soft Matter* **2011**, *7*, 2632-2638.

(38) Landau, L. D.; Lifshitz, E. M. Theory of elasticity 3rd edition. **1986**.

(39) Kimishima, K.; Koga, T.; Hashimoto, T. Order−order phase transition between spherical and cylindrical microdomain structures of block copolymer. I. mechanism of the transition. *Macromolecules* **2000**, *33*, 968-977.

(40) Seguela, R.; Prud'homme, J. Affinity of grain deformation in mesomorphic block polymers submitted to simple elongation. *Macromolecules* **1988**, *21*, 635-643.

Chapter 4

Effect of multiaxial deformation modes on microphase-separated structure of styrenic triblock copolymer

4.1 Introduction

To investigate the deformation mechanism of SEBS, effect of deformation mode on mechanical properties and the microphase-separated structure of the sample is another important point to be taken into account. There are various common mechanical deformation modes, including uniaxial stretching, equi-biaxial stretching, planar extension[1-3], shear, compression[4-5] and bulge tests[6-11]. Deformation of SEBS during uniaxial and equi-biaxial stretching were investigated in Chapter 2. Compression and bulge tests are considered multiaxial deformation modes. Apart from a well-known equi-biaxial testing. these two modes are useful to understanding the mechanical propertied of polymer films as the deformation conditions are quite similar to practical applications. Small amount of sample was required to perform the compression and bulge test. Deformation behaviors of the sample during bulge test was proposed to be equivalent to the compression test as extension in multi-directions together with one-dimensional compression occurred during both deformation modes. However, the applied force was in the different direction. Moreover, the deformation in edge view of compressed sample was proposed to relate to transverse direction of equi-biaxial stretching, which occurred to keep the volume constant.

In this chapter, microphase-separated structure of SEBS during equi-biaxial stretching was compared to compression and bulge tests using in situ SAXS measurement. An arrangement and deformation of PS domains during these three modes would be discussed.

4.2 Experiment

The procedure of the sample preparation was explained in section 2.2.1. Specimens were cut into a rectangular shape with dimensions of 20×20 mm^2 for equi-biaxial and

15×15 mm^2 for bulge test. For compression test, SEBS films were stamped into cylindrical shape with diameter of 3 mm. Experimental set-up of equi-biaxial stretching was described in Chapter 1. Figures 4.1 (a) and (b) illustrated the set-up of SEBS during compression and bulge tests, respectively. For compression testing, the specimen was set between parallel sapphire glasses and compressed at 10 μm s^{-1}. For bulge testing, and experimental set-up have been described in detail elsewhere.[10] Pressure was applied with a rate of 0.2 kPa s^{-1}. The synchrotron radiation X-ray scattering measurements were conducted with the BL05XU beamlines in the SPring-8 facility in Japan. Figure 4.2. shows schematic illustration of experimental set-up of *in situ* SAXS measurements during equi-biaxial stretching, compression and bulge testing. The beam size at the samples was 150 × 150 μm^2. The wavelength of the X-ray was 0.100 nm, and the sample-to-detector distance was 4 m for SAXS. Samples were exposed to the X-ray beam for 0.5-1 s at ambient temperature. For bulge test, SAXS patterns were taken with the beam perpendicular to the film surface (through view). For compression test, SAXS patterns were taken with the beam perpendicular to the film surface (through and edge view). 2D-scattering patterns of SAXS were obtained from a PILATUS 1M detector (DECTRIS Ltd) with a total pixel size of 172 × 172 μm^2. Data were converted from 2D patterns to 1D profile by integrating with FIT2D (ver. 16.041, Andy Hammersley/ESRF, Grenoble, France).

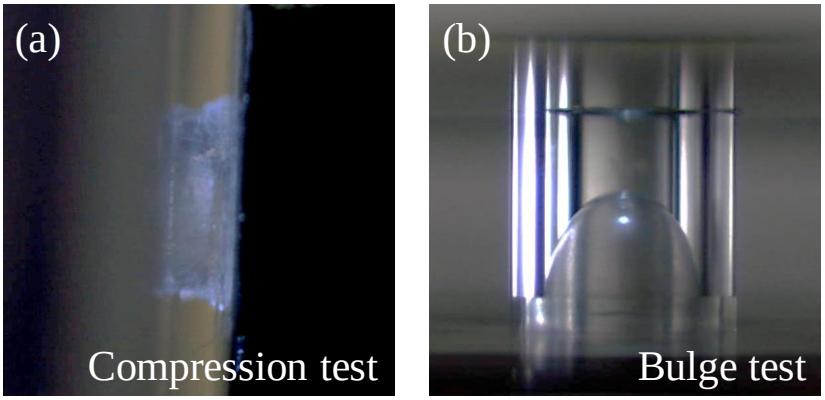

Figure 4.1. Experimental set up of SEBS during (a) compression and (b) bulge tests.

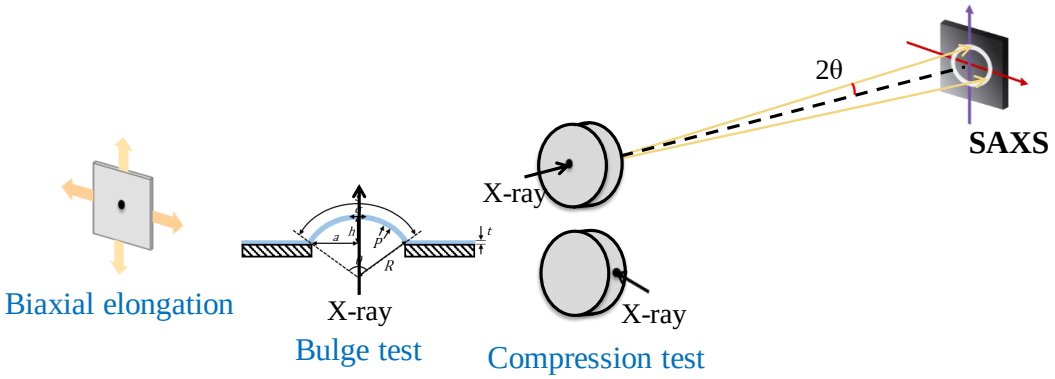

Figure 4.2. Schematic illustration of experimental set-up of *in situ* SAXS measurements during equi-biaxial stretching, compression and bulge testing.

4.3 Results and discussion

4.3.1 Stress-strain relationship

Figure 4.3 displays stress-strain curves of equi-biaxial stretching, compression and bulge tests. Stress and strain of bulge test were calculated from the following equation:[11]

$$Stress\ (\sigma) = \frac{PR}{2t} = \frac{P(a^2+h^2)}{4th} \tag{4.1}$$

$$Strain\ (\varepsilon) = \frac{s-s_0}{s_s} \tag{4.2}$$

$$s = \theta R = \tan^{-1}\left(\frac{h}{a}\right)\frac{2(a^2+h^2)}{h} \qquad (4.3)$$

where s is the arc length, s_0 is the initial arc length, P is the applied pressure, h is the bulge height, t is the sample thickness, a is the film radius, and θ and R are the angle and the bulge radius of curvature, respectively. Samples of equi-biaxial stretching and bulge tests were stretched until ruptured. Samples under bulge test was considered to deform in multiaxial directions. Equi-biaxial stretching and bulge tests showed almost same initial modulus. However, equi-biaxial stretching showed larger strain at break than that of bulge test, which could be because larger entanglement effect of PEB chains during multiaxial stretching of bulge test. For compression test, the sample was compressed to strain -0.9 to observe the stress. Minus sign of strain refers to the opposite direction to the stretching direction of other deformation modes.

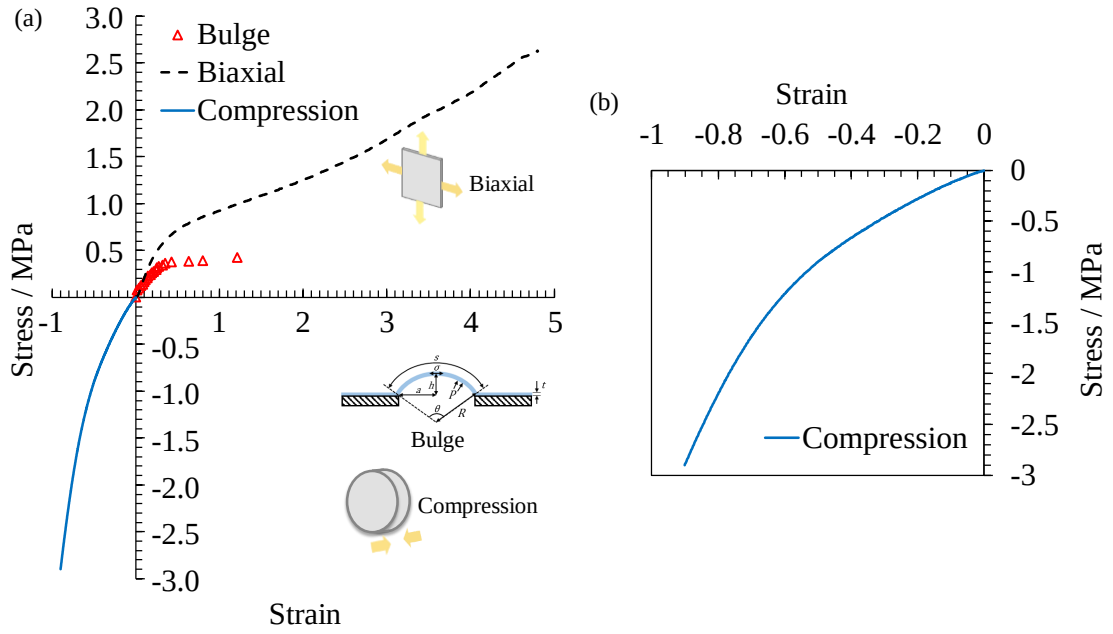

Figure 4.3. (a) Stress-strain curves of SEBS samples during equi-biaxial stretching, bulge and compression tests at 25 °C. (b) Magnified stress-strain curve of compression test.

4.3.2 Microdomain structure change of SEBS during various deformation modes

In situ SAXS measurement was performed during equi-biaxial stretching, compression, and bulge tests. Equi-biaxial stretching results which was discussed in Chapter 1, was adopted to compare the deformation behaviors with compression and bulge tests as they are multiaxial deformation modes. Figures 4.4, 4.5, 4.6 and 4.7 show 2D SAXS patterns and 1D SAXS profiles of SEBS during equi-biaxial stretching, bulge, and edge and through view of compression tests, respectively. For bulge test, an observation position was at the center of the sample as it was proposed to be the position that sample was deformed isotropically in multiaxial directions. SAXS results were analyzed from X- and Y-axes for comparing the results from two different directions. It was found that three diffraction peaks of SEBS shifted to lower *q* region in two directions during equi-biaxial stretching, bulge test and through view of compression tests. On the other hand, the diffraction peaks shifted to higher and lower *q* region in compressing and transverse direction, respectively. This shift of the diffraction peaks insists that domain spacing of PS domains increased with increasing strain during equi-biaxial stretching, bulge, and through view of compression tests. For edge view of compression test, the spacing of PS domains decreased and increased in compressing and transverse directions, respectively. Deformation of the sample in through view of compression test was considered to be same as under equi-biaxial stretching. The sample was totally attached to the sapphire glasses during compression test, leading to the possibility that the compressive force on each position of the sample was equivalent. Different characteristic of 2D SAXS patterns was found in each deformation mode. Explanation was discussed based on the calculation of scattering pattern using Fast Fourier Transform (FFT). The calculated patterns are shown in the Appendix of Chapter 2 (Figures 2A.1 to 2A.3). Scattering patterns are related to the characteristic features of reflection planes of the

paracrystalline lattice.[12] In the case that the size of grain is much larger than beam size, a dot-like pattern is observed. In contrast, a line-like pattern emerges when the size of grain is smaller. For equi-biaxial stretching and compression test, the ring pattern contained dot-like and line-like characteristics when the sample was stretched. Due to the random-oriented multigrain structure of SEBS, it is feasible that different sizes of grain occurred, resulting in the combination of two types of patterns. For bulge tests, dot-like characteristic was obviously observed from 2D SAXS patterns, indicating that large grain occurred during deformation. The different characteristic of 2D SAXS patterns of equi-biaxial stretching, compression and bulge test suggest that biaxial and multiaxial deformation affect the deformation in mesoscopic structure of SEBS.

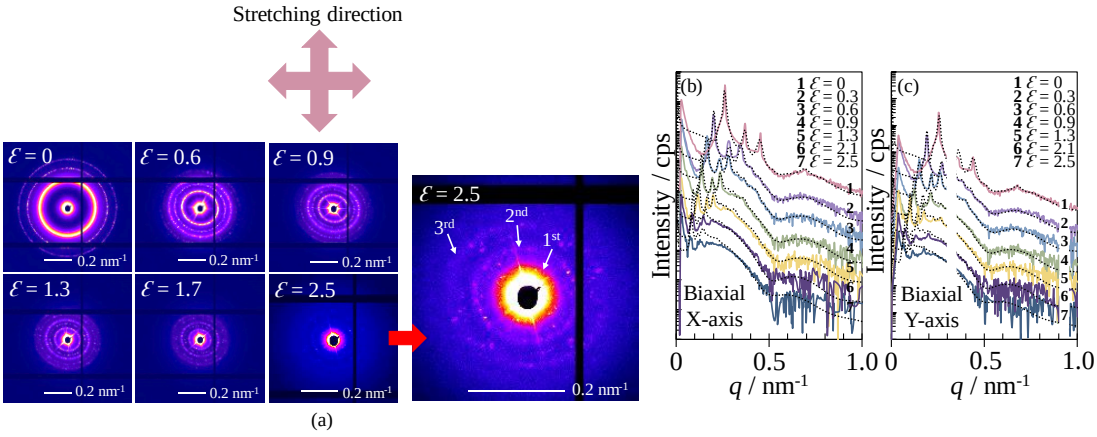

Figure 4.4. (a) 2D SAXS patterns of SEBS during equi-biaxial stretching at 1 mm s^{-1} and 25 °C at various strains with the beam perpendicular to the film surface (through view). (b) 1D SAXS profiles obtained from (a) in the X-axis and (c) Y-axis. Black dot lines were obtained from the model calculation.

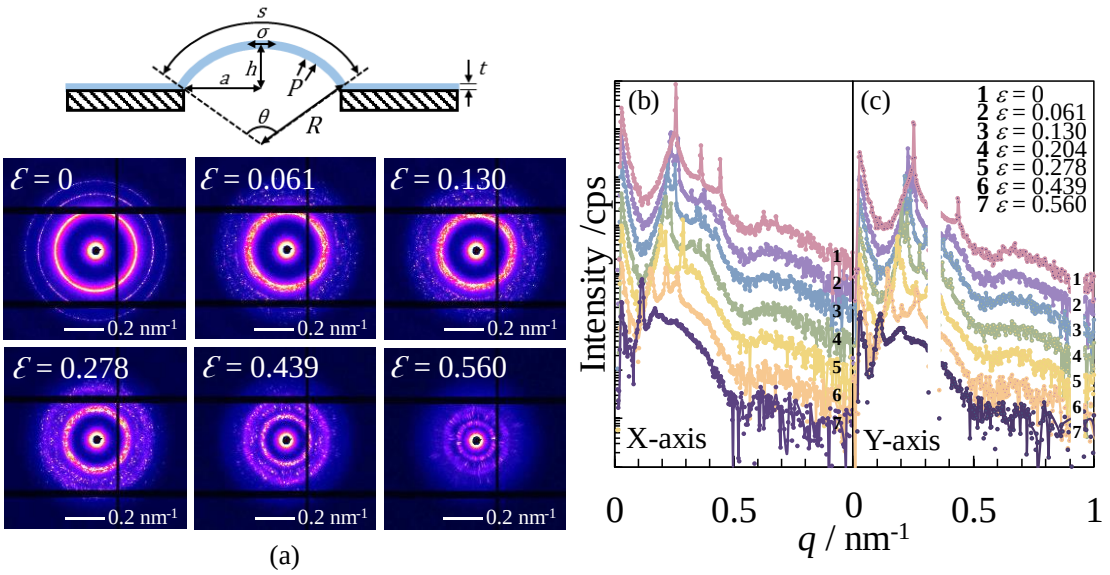

(a)

Figure 4.5. (a) 2D SAXS patterns of SEBS during bulge test at 25 °C at various strains with the beam perpendicular to the film surface (through view). (b) 1D SAXS profiles obtained from (a) in the X-axis and (c) Y-axis.

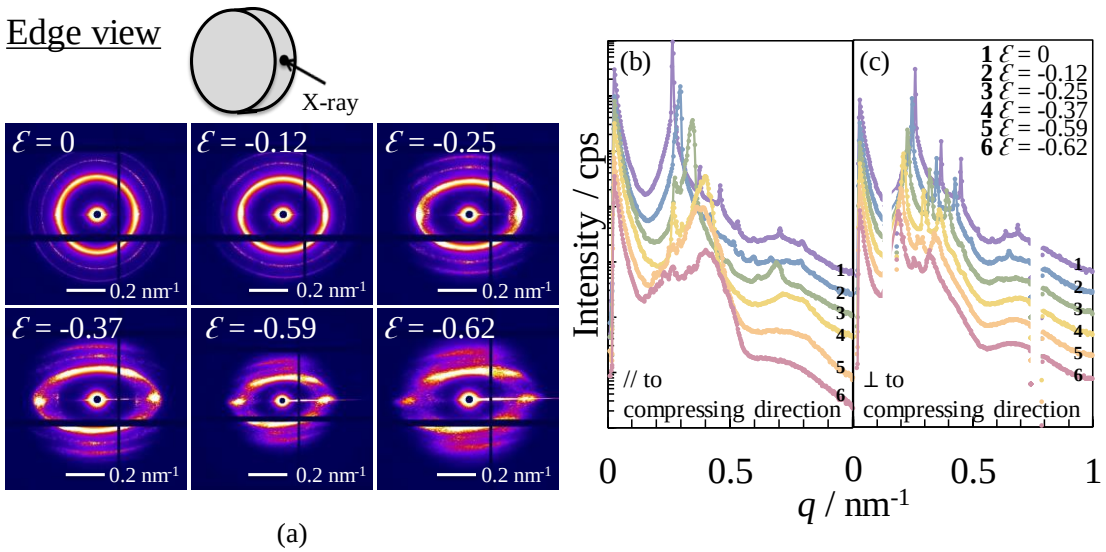

(a)

Figure 4.6. (a) 2D SAXS patterns of SEBS during compression test at 10 μm s^{-1} and 25 °C at various strains with the beam perpendicular to the film surface (edge view). (b) 1D SAXS profiles obtained from (a) in the compressing and (c) transverse directions.

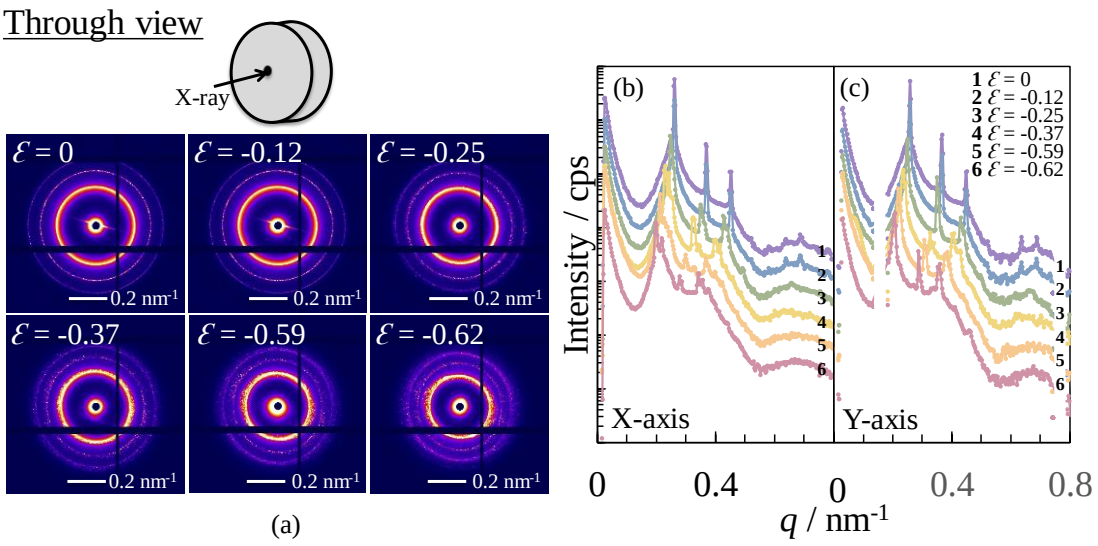

Figure 4.7. (a) 2D SAXS patterns of SEBS during compression test at 10 μm s^{-1} and 25 °C at various strains with the beam perpendicular to the film surface (through view). (b) 1D SAXS profiles obtained from (a) in the compressing and (c) transverse directions.

4.3.3 Arrangement and deformation of PS domains

Figures 4.8 (a) and (b) illustrate relationship between real strain and $\Delta d/d_0$, and average length of semiaxes of PS domains during bulge test. It was found that SEBS during bulge test show affine deformation until strain 3. This trend indicates that simple arrangement of PS domains occurred during multiaxial deformation of bulge test. However, $\Delta d/d_0$ was larger than real film strain after strain 3. Before the sample was ruptured by the applying pressure, deformation of the SEBS film rapidly increased. After strain 3 until ruptured, larger $\Delta d/d_0$ could be because irreversible phenomena, such as rupture of PEB chains and PS domains, occurred from the rapid increase of film strain. The deformation of PS domains during bulge test was clarified from form factor results. The form factor shifted toward the lower q region in both the X- and Y-axis, indicating isotropic deformation along the two axes of the stretching directions. These results verify the transformation of spherical PS domains to oblate spheroids during bulge test.

Calculation method was described in Chapter 2. Average length of semiaxes of PS domains increased after the film sample was initially stretched by the applied pressure and remained constant. It can be stated that an increasing in film strain during bulge test led to an increase in domain spacing. However, deformation of PS domains occurred only in the initial state of film deformation. Large entanglement effect of the PEB chains during bulge test might be a reason that limit the deformation of PS domains.

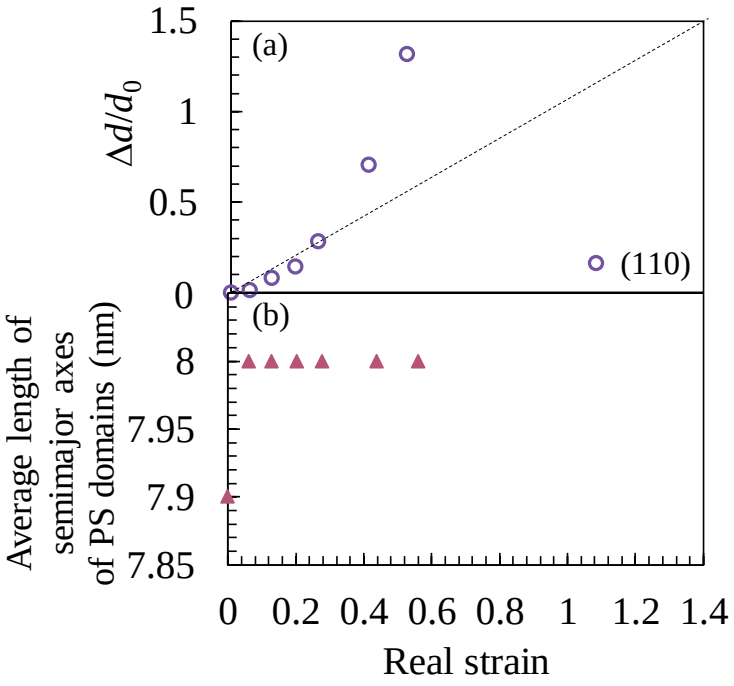

Figure 4.8. Deformation behaviors of SEBS during bulge test with increasing strain. (a) Relationship between real strain and $\Delta d/d_0$. (b) Average length of semiaxes of PS domains.

Figures 4.9 (a), (b), (c), and (d) illustrate relationship between real strain and $\Delta d/d_0$ in compressing and transverse direction of edge view, through view, and average length of semiaxes of PS domains during compression test. It was found that SEBS did not exhibit affine deformation, which might be because PS domains cannot arrange

themselves well during the compression force. The deformation of PS domains during compression test was elucidated from form factor results. As both edge and through views can be obtained from compression test, deformation of PS domains in three-dimension was investigated. In edge view, the form factor shifted toward the higher and lower q region in compressing and transverse direction, respectively. In case of through view, the form factor shifted toward the lower q region in both the X- and Y-axis, indicating isotropic deformation along the two axes. These results confirm the transformation of spherical PS domains to oblate spheroid during compression test. Semimajor and semiminor axes were calculated from the form factor of edge view in compressing direction and through view, respectively. The semiminor axis of oblate spherical PS domains clearly increased, while the semimajor axis decreased with increasing strain, as shown in Figure 4.9 (d).

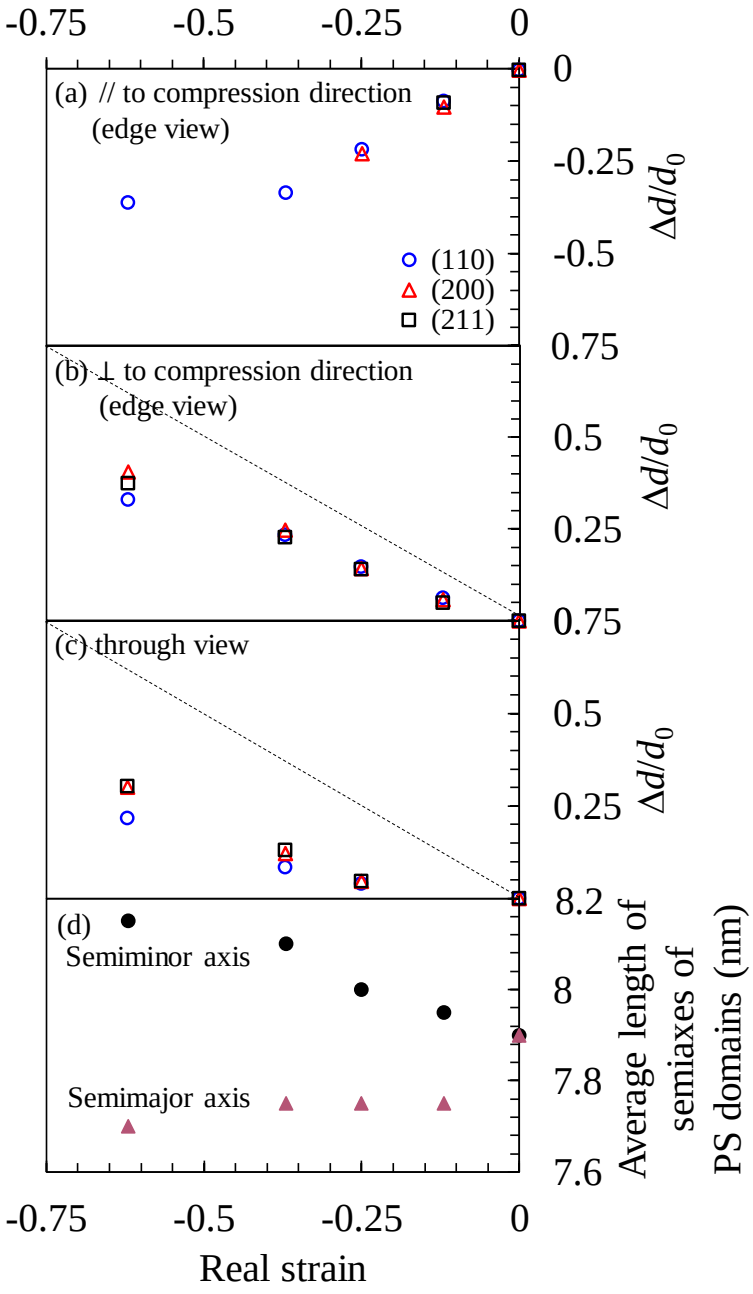

Figure 4.9. Deformation behaviors of SEBS during compression test with decreasing strain. Relationship between real strain and $\Delta d/d_0$ (a) edge view of compressing direction. (b) edge view of transverse direction. (c) through view of compression test. and (d) Average length of semiaxes of PS domains.

4.4 Conclusions

An arrangement and deformation of PS domains during compression and bulge tests were investigated to compare with equi-biaxial stretching using *in situ* SAXS measurement. Bulge tests was considered a multiaxial deformation, while compression test and equi-biaxial stretching were similar. Different characteristics in 2D patterns three deformation modes were observed. Dot-like patterns were clearly observed in the 2D patterns of the bulge test, indicating that large grains mostly occurred in SEBS during multiaxial deformation mode. On the contrary, the combination of dot-like and line-like patterns was observed during equi-biaxial stretching and compression test, suggesting that different size of gain occurred when SEBS was stretched simultaneously in only two directions. Simple arrangement of PS domains was observed at small strain during equi-bixial stretching and bulge tests, however, it was not observed in both view of compression test. This result indicates an effect of the direction of applied force in the sample deformation. In all deformation modes, spherical PS domains transformed to oblate spheroid. The deformation of PS domains during bulge test occurred only in the initial state. Large entanglement effect of the PEB chains during bulge test might be a reason that limit the deformation of PS domains. For compression test, the semimajor and semiminor axes increased and decreased with increasing strain.

References

(1) Urayama, K.; Ogasawara, S.; Takigawa, T. Pure shear deformation of physical and chemical gels of poly(vinyl alcohol). *Polymer* **2006**, *47*, 6868-6873.

(2) Mai, T.-T.; Morishita, Y.; Urayama, K. Novel features of the Mullins effect in filled elastomers revealed by stretching measurements in various geometries. *Soft Matter* **2017**, *13*, 1966-1977.

(3) Mai, T.-T.; Matsuda, T.; Nakajima, T.; Gong, J. P.; Urayama, K. Distinctive characteristics of internal fracture in tough double network hydrogels revealed by various modes of stretching. *Macromolecules* **2018**, *51*, 5245-5257.

(4) Chen, P.; Xie, H.; Huang, F.; Huang, T.; Ding, Y. Deformation and failure of polymer bonded explosives under diametric compression test. *Polymer Testing* **2006**, *25*, 333-341.

(5) Chai, A. B.; Andriyana, A.; Verron, E.; Johan, M. R.; Haseeb, A. S. M. A. Development of a compression test device for investigating interaction between diffusion of biodiesel and large deformation in rubber. *Polymer Testing* **2011**, *30*, 867-875.

(6) Vendamme, R.; Onoue, S.-Y.; Nakao, A.; Kunitake, T. Robust free-standing nanomembranes of organic/inorganic interpenetrating networks. *Nature Materials* **2006**, *5*, 494-501.

(7) Huang, C. K.; Lou, W. M.; Tsai, C. J.; Wu, T.-C.; Lin, H.-Y. Mechanical properties of polymer thin film measured by the bulge test. *Thin Solid Films* **2007**, *515*, 7222-7226.

(8) Machado, G.; Chagnon, G.; Favier, D. Analysis of the isotropic models of the Mullins effect based on filled silicone rubber experimental results. *Mechanics of Materials* **2010**, *42*, 841-851.

(9) Watanabe, H.; Fujimoto, A.; Nishida, J.; Ohishi, T.; Takahara, A. Biobased polymer coating using catechol derivative urushiol. *Langmuir* **2016**, *32*, 4619-4623.

(10) Kojio, K.; Nagano, C.; Fujimoto, A.; Nozaki, S.; Yokomachi, K.; Kamitani, K.; Watanabe, H.; Takahara, A. In situ synchrotron radiation X-ray diffraction studies on molecular aggregation structure of nylon 12 films during bulge testing. *Soft matter* **2018**, *14*, 1659-1664.

(11) Kojio, K.; Fujimoto, A.; Kajiwara, T.; Nagano, C.; Masuda, S.; Cheng, C.-H.; Nozaki, S.; Kamitani, K.; Watanabe, H.; Takahara, A. Advantages of bulge testing and rupture mechanism of glassy polymer films. *Polymer* **2019**, *179*, 121632.

(12) Hosemann, R.; Bagchi, S., Direct analysis of diffraction by matter. North-Holland Pub. Co.: 1962.

Chapter 5

Conclusions

Conclusions

In situ synchrotron radiation SAXS measurements revealed a change in the microphase-separated structure of SEBS during various deformation modes. In Chapter 2, an orientation of the PEB chains as well as an arrangement and deformation of PS domains were investigated. WAXS measurements revealed the orientation of the PEB chains during uniaxial stretching only at high strain region, however, no orientation was found during equi-biaxial stretching. From SAXS results, spherical PS domains transformed to prolate spheroids during uniaxial stretching and to oblate spheroids during equi-biaxial stretching. Both deformation modes similarly followed the affine deformation up to the certain strain ($\mathcal{E}_{d\text{-A}}$) due to the simple arrangement of PS domains and the extension of PEB chains. Ordering of PS domains decreased upon stretching. Above $\mathcal{E}_{\text{d-A}}$, PS domains came into contact with each other in the transverse direction, and the distance between PS domains reached the maximum length of PEB chains in the fully-extended state, leading to irreversible phenomena in the sample. The plane-independent phenomenon was still occur during uniaxial stretching, however, equi-biaxial stretching showed plane-dependent phenomenon. Equi-biaxial stretching showed a lower $\mathcal{E}_{\text{d-A}}$ than uniaxial stretching due to entanglement effect of PEB chains. After contact of PS domains, ordering suddenly increased at around strain 6 and 2 during uniaxial and equi-biaxial stretching, respectively, due to the release of locked state of PS domains and extended PEB chains. This is explained based on the sudden change in FWHM of the (211) diffraction peak and shift to smaller plane spacing.

In Chapter 3, the mechanical stretching behavior of SEBS was investigated under three different stretching modes and through *in situ* SAXS analysis. The cross-effect of strain represented by second invariants of the deformation tensor (I_2) was identified, and only the Ogden model could be used to fit the data. In the cyclic stretching test, SEBS

exhibited smaller hysteresis and deviation from the affine deformation during cyclic equi-biaxial stretching than that during uniaxial stretching. The cross-effect of strains in different directions may be attributed to the (1) existence of three different lengths of PEB bridge chains between PS domains, (2) pulling out of PS end blocks from PS domains, and (3) presence of the entangled loop. The entangled loop effect might be the main factor for small hysteresis and deviation from affine deformation during equi-biaxial stretching.

In Chapter 4, an arrangement and deformation of PS domains during compression and bulge tests were investigated to compare with equi-biaxial stretching using *in situ* SAXS measurement. Bulge test was considered a multiaxial deformation, while SEBS under compression test was considered a biaxial stretching test. Simple arrangement of PS domains was observed at small strain during equi-bixial stretching and bulge tests, however, it was not observed in both view of compression test. This result indicates an effect of the direction of applied force in the sample deformation. In all deformation modes, spherical PS domains transformed to oblate spheroid. The deformation of PS domains during bulge test occurred only in the initial state. Large entanglement effect of the PEB chains during bulge test might be a reason that limit the deformation of PS domains. For compression test, the semimajor and semiminor axes increased and decreased with increasing strain.

From these studies, the results showed that glassy PS domains deformed during various deformation modes. This deformation could be because low molecular weight of PS in SEBS sample in this study. To improve the mechanical properties of SEBS, an increase in rigidity of PS domains was suggested. Possible ways might be an increase in molecular weight of the domains and the addition of some miscible polymer into the PS domains to increase the toughness of the sample.

ACKNOWLEDGMENTS

I would like to express my gratitude to my supervisor, Prof. Atsushi Takahara, for giving me the great opportunity to join his research group, precious guidance, support as well as generous encouragement. My appreciation and sincerity pass to Assoc. Prof. Ken Kojio for his support, dedication, encouragement, constructive suggestions and comments. Also, I would like to extend thanks to Asst. Prof. Yoshifumi Amamoto for his kind support and suggestion.

I would like to thank other two members of my dissertation committee, Prof. Keiji Tanaka and Prof. Tsuyohiko Fujigaya for generously offering their time, support and guidance to this dissertation.

I gratefully acknowledge to the grant from International Graduate Course on Chemistry for Molecular Systems, Ministry of Education, Culture, Sports, Science and Technology (MEXT), Japan for providing the scholarship throughout my doctoral program.

I would like to acknowledge the support from Prof. Hiroshi Jinnai and Asst. Prof. Hsiao-Fang Wang from Tohoku University for their investigation on TEM micrographs of SEBS. BL05XU and BL40XU beamlines in the SPring-8 facility in Japan are also acknowledged for the synchrotron radiation X-ray scattering experiments.

Many thanks go to Assoc. Prof. Yuji Higaki, Dr. Kazutaka Kamitani, Dr. Masaru Mukai, Dr. Yucheng Zhang, Dr. Shuhei Nozaki, Dr. Masanao Sato, Dr. Rahmawati, Chao-Hung Cheng, Nobuhisa Takayama, Chigusa Nagano, Yoshihiro Inutsuka, Tatsunori Sakamaki, Shiori Masuda, Hitoshi Shimamoto, Kento Fukuda, Kosuke Ikata, Naoki Okawa as well as Takahara lab’s members who are not mentioned here for their kind assistance in various ways and memorable friendships. The kind supports from Aya

Fujimoto, Tomoko Kajiwara, Keiko Higaki, Yoko Iki, Ayumi Hamada, Aiko Miyamoto, Motoko Teranishi as well as all staffs in Takahara lab are also appreciated.

My appreciation also extends to Asst. Prof. Thasaneeya Kuboki for her kindness and emotional support. I gratefully thank to Rachanon Chaiuppala, Dr. Chitiphon Chuaicham, Dr. Chacriya Malasuk, Dr. Onchanok Juntarasakul and all Thai friends in Fukuoka for their warmth, cheerfulness and wonderful friendship as always. Weeradet Sittiphon and Dr. Natsuda Klongvessa are acknowledged for their kind suggestions on the mathematics and physics calculations. Danaikarn Jongfuangprinya is another person I would like to thank for emotional support and his suggestion on artworks.

Last but not least, I would like to take this opportunity to express my greatest gratitude to my lovely parents and family for their endless love, inspiration, patience and emotional support. I can go through my tough times from their encouragement. All of my successes dedicate to my parents who always give me the best thing.